Andean Geology 53 (1): 1-33. January, 2026
doi: 10.5027/andgeoV53n1-3777

Andean Geology
www.andeangeology.cl

Late Miocene slope calcareous tufa, Atacama Desert, Chile: the role of faults, groundwater movement, and climate

***Carol de Wet[1], Linda Godfrey[2], Catherine Caterham[3], Andrew de Wet[1], Sabrina R. Brown[4], Dylan Lee[5], Connor Hicks[6], Lauren Mumby[7]**

[1] *Department of Earth and Environment, Franklin & Marshall College, 415 Harrisburg Pike, Lancaster, PA USA.*
cdewet@fandm.edu, adewet@fandm.edu
[2] *Department of Earth and Planetary Sciences, Rutgers University, 610 Taylor Road, Piscataway, NJ USA.*
linda.godfrey@rutgers.edu
[3] *Department of Earth, Environmental, and Planetary Sciences, University of Tennessee, 602 Strong Hall, 1621 Cumberland Ave., Knoxville, TN USA.*
ccaterha@vols.utk.edu
[4] *Niswander Department of Biology, Manchester University, 604 E College Ave., North Manchester, IN USA.*
srbrown@manchester.edu
[5] *Department of Earth and Marine Sciences, University of North Carolina, Mitchell Hall, 104 South Road, Chapel Hill, NC USA.*
dlee41@unc.edu
[6] *Roux Associates, 402 Heron Drive, Logan Township, NJ USA.*
chicks@rouxinc.com
[7] *Department of Earth Science, University of California, 1006 Webb Hall, Santa Barbara, CA USA.*
laurenmumby@ucsb.edu

** Corresponding author: cdewet@fandm.edu*

ABSTRACT. This study enhances our understanding of Late Miocene-Pliocene climate in the Atacama Desert of the Antofagasta Region in northern Chile. Field relations, petrography, and geochemistry from two previously undescribed, fossil springs within the Calama Basin's Opache Formation demonstrate similarities between the springs, such as laminated crystalline carbonate, including freshwater aragonite botryoids, but differences in trace element and δ^{13}C values. One location contains stromatolites, oncolites, and sedimentary structures indicative of flowing water including ripple marks and microterracettes, whereas such features are generally absent at the other site. Both study areas are associated with fault systems that transferred groundwater from regional aquifers to the surface, bringing water rich in strontium, magnesium, iron, and manganese, to coprecipitate with $CaCO_3$ as either aragonite or calcite. This correlation between springs and tectonics is becoming more widely recognized in other continental settings.

Keywords: Tufa, Springs, Atacama, Geochemistry, Faulting.

RESUMEN. Tobas calcáreas de vertientes del Mioceno Superior, Desierto de Atacama, Chile: el rol de las fallas, movimiento de agua subterránea y clima. Este estudio presenta nuevos antecedentes sobre el clima del Mioceno Superior- Plioceno en el altiplano de la región de Antofagasta, norte de Chile. La información de campo, petrográfica y geoquímica de dos vertientes fósiles contenidas en la Formación Opache, no descritas anteriormente, muestra similitudes, por ejemplo, la presencia de carbonato cristalino laminado (que incluye botrioides de aragonito de agua dulce), pero diferencias en su contenido de elementos traza y δ^{13}C. Uno de los sitios contiene estromatolitos, oncolitos y estructuras sedimentarias de flujo, que incluyen ondulitas y microterracetas, los cuales están típicamente ausentes en el otro. Ambos sectores están asociados a sistemas de fallas que han transferido agua subterránea desde acuíferos regionales a la superficie, transportando agua rica en estroncio, magnesio, hierro y manganeso, la cual coprecipitó con $CaCO_3$ en forma de aragonito o calcita. Esta correlación entre vertientes y tectónica se está reconociendo cada vez con más frecuencia en otros ambientes continentales.

Palabras clave: Toba, Manantiales, Atacama, Geoquímica, Fallas.

1. Introduction

Deepening an understanding of the Atacama Desert region's past hydrologic system is important in an area where water is a precious resource. Ancient spring deposits represent sites where groundwater once emerged at the land surface, so their study may provide insight into potential new groundwater flow paths if reactivated by tectonic or climatic factors. Copper mining and other mineral extraction require large quantities of water, and export of these minerals makes up a significant portion of the Chilean economy, thus understanding regional water distribution is economically relevant. In addition, rural communities of northern Chile have relied on springs as an essential source of freshwater, and villages are often located near spring sites (Houston, 2007; C. de Wet, personal observation), so new antecedents on ancient spring dynamics may be useful for future generations.

Freshwater carbonates represent a detailed record of their environmental depositional conditions, particularly in hyperarid, arid, and semi-arid regions where diagenetic alteration is minimal (*e.g.*, Ashley *et al.*, 2014; de Wet *et al.*, 2022). The Atacama Desert's present hyperaridity means that carbonate deposits there are well preserved and provide a detailed record of past shifts in regional precipitation and/or subsurface groundwater circulation. Previous research on the ~42 km^2 Opache Formation in the Calama Basin (Fig. 1), of the Antofagasta Region, which consists of alluvial gravels, sandstones, and lacustrine to palustrine limestones (May, 1997; Blanco and Tomlinson, 2009; Álvarez *et al.*, 2023), demonstrates that over the past ~8 Myr, the area around the city of Calama has experienced periods of higher precipitation than today (de Wet *et al.*, 2015, 2019). Three spring-sourced, carbonate-depositing rivers are still active in the area today: the Loa, Salado and San Salvador rivers (Fig. 1). Carbonate deposition in these rivers is expressed as barrage tufas, rhizoconcretions, and flowstone deposits (de Wet *et al.*, 2022). As similar features are preserved in Late Miocene and younger limestones (de Wet *et al.*, 2015, 2019, 2022), the processes interpreted from the rock record are still operating today, albeit at a reduced scale.

In the present study, we examine two Late Miocene carbonate spring deposits within the Opache Formation to further understand freshwater carbonate deposition in the Atacama Desert of the Antofagasta Region. The studied limestones are from El Sifón, a location near the village of Ayquina, in the Turi Basin (a sub-basin within the Calama Basin; Houston, 2007), the other is located at Chintoraste in the Calama Basin (Fig. 1). These previously undescribed tufas share some common characteristics: layered to laminated, <1 m-thick crystalline aragonite and/or calcite horizons, brecciated carbonate layers, botryoidal crystal mamelons lining cavities, and detrital silty sandstone to mudstone beds. Aragonite is the predominant carbonate polymorph at El Sifón, while calcite is the most abundant mineral phase at Chintoraste. This study examines the two deposits to gain insight into the interplay of tectonics and groundwater flow in generating tufa, and supports previous research on the Opache Formation which described the Late Miocene as a sub-epoch when this part of the Atacama Desert was intermittently wetter than today, experiencing arid to semi-arid conditions, thereby facilitating extensive palustrine and lacustrine environments (de Wet *et al.*, 2015, 2019).

The two fossil springs deposits studied here show that they formed as fissure-ridge, or vein-fed tufas which were linked to groundwater moving

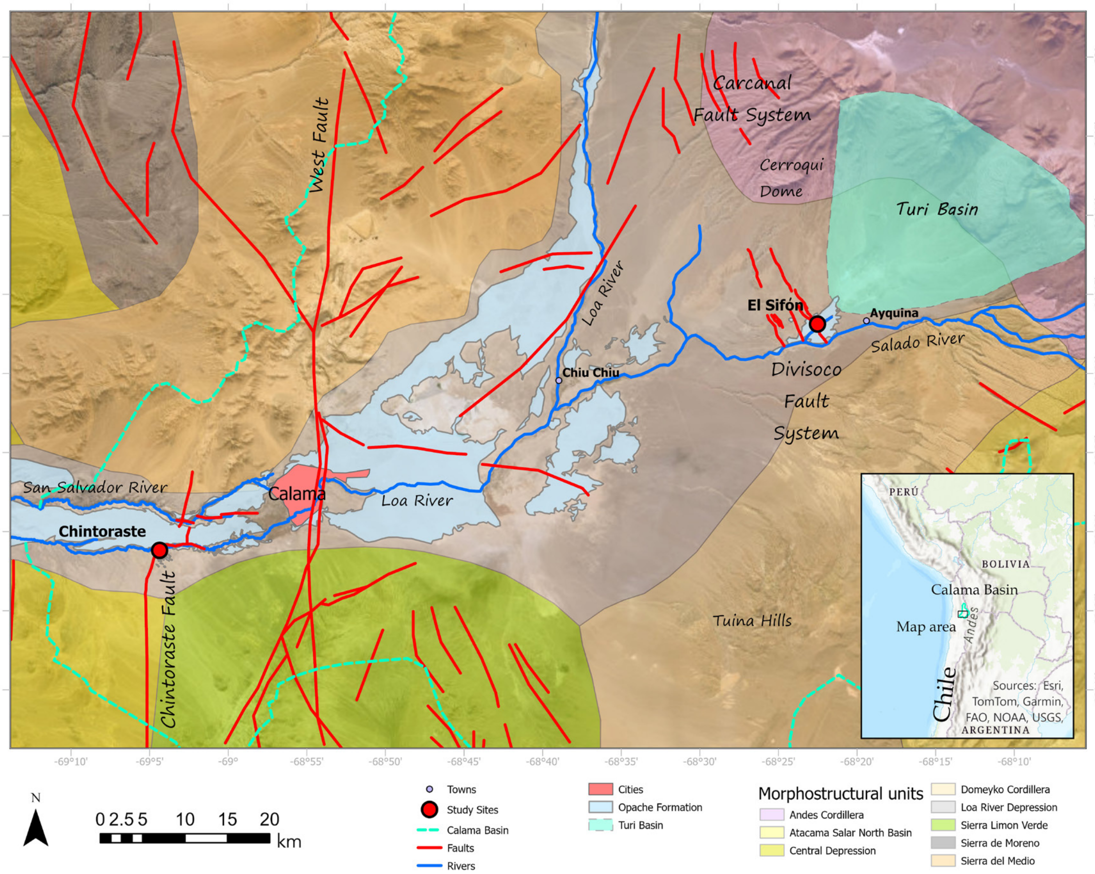

FIG. 1. Morphostructural map of the study area. Units extracted from the 1:100,000-scale geological maps of Cupo-Toconce (Álvarez *et al.*, 2023), Sierra Gorda (Duhart *et al.*, 2018), and Calama (Tomlinson *et al.*, 2018). The study sites are shown as red circles. Background image from the World Imagery ArcGIS Map Service.

along regional faults. Martini and Capezzuoli (2014) suggested that such tufas may serve as a proxy for tectonics, indicating where potentially unknown faults intersect aquifers. Ashley *et al.* (2014) provided new insight into intrabasinal fault distribution and potable water sources by studying fault-related springs in Olduvai Gorge, Tanzania. Hence, increasing our knowledge on fossil tufa distribution in the tectonically active Atacama Desert region has the potential to indicate where new springs might form if active faults tap into aquifers, providing new sources of water for the surface environment or human use.

It is worth mentioning that there is a lack of consensus on travertine and tufa terminology. Although these carbonates require meteoric water input, a supply of CO_2, carbonate ions, and environmental conditions favorable to their deposition and preservation, they can form in a range of continental environments (*e.g.*, Pedley, 1990; Ford and Pedley, 1996; Camuera *et al.*, 2015). Those associated with waters warmer than ambient temperatures may be termed travertine (Ford and Pedley, 1996; Jones and Renaut, 2008; Alonso-Zarza *et al.*, 2021), whereas those deposited from ambient temperature fluids are generally referred to as tufa (see Pentecost, 2005, and Jones and Renaut, 2010, for discussion). In this study none of the carbonates had oxygen isotopic values indicative of hot water deposition, therefore, the term tufa is applicable and is used here.

2. Geologic setting

The Calama Basin area can broadly be separated into east and west morphostructural units (Tomlinson *et al.*, 2018) (Fig. 1). The eastern unit is the modern (Late Cenozoic) arc, consisting of andesitic to dacitic volcanoes and domes, and andesitic to rhyodacitic ignimbrites (Sellés and Gardeweg, 2017; Bertin and Amigo, 2019; Álvarez *et al.*, 2023). While many of the volcanoes in the Turi Basin area, where El Sifón is located, post-date the spring deposits, a few were likely contemporaneous with spring deposition (*e.g.*, Cerro Carcanal, Cerro Negro). The >20,000 km^2 Sifón Ignimbrite, which in the study area underlies the Opache Formation carbonates, was deposited sometime between 9 and 7.5 Ma (Sellés and Gardeweg, 2017; Tomlinson *et al.*, 2018; Bertin and Amigo, 2019; Álvarez *et al.*, 2023). Most of the rocks that underlie the modern arc deposits are obscured by the voluminous Late Miocene-Pliocene ignimbrites; however, Permian-Triassic and Cretaceous volcanic and siliciclastic sedimentary rocks have been described in the nearby Tuina hills (Henríquez *et al.*, 2014; Álvarez *et al.*, 2023) (Fig. 1). The geology to the west, where the Chintoraste spring is located, is more varied. In fact, Devonian-Permian metamorphic, Carboniferous-Triassic volcanic and plutonic, Jurassic-Cretaceous sedimentary, and Cretaceous-Paleogene volcano-sedimentary and plutonic rocks outcrop around Chintoraste and the nearby city of Calama (Duhart *et al.*, 2018; Tomlinson *et al.*, 2018).

The spring tufas at El Sifón and Chintoraste are situated on or adjacent to mapped faults (Fig. 1). El Sifón lies on the Late Miocene, high-angle dextral transtensional Divisoco Fault System (Álvarez *et al.*, 2023). This fault system strikes NNW, and meets up with the similarly trending, but younger and sinistral strike-slip Carcanal Fault System in the vicinity of the Cerroqui Dome (Álvarez *et al.*, 2023). Chintoraste, on the other hand, occurs ~1 km to the east of the NNE-striking, east-vergent, high-angle reverse Chintoraste Fault, which separates the Eocene Icanche Formation from marine Jurassic sediments (Duhart *et al.*, 2018). The Opache Formation rocks cover part of the fault trace in the Chintoraste area. About 1 km to the SE of the spring site, a ~1.5 km-long, NNE-striking and east-dipping fault brought the same marine Jurassic sediments to the surface (Duhart *et al.*, 2018). Orthogonal to the Chintoraste Fault, Jordan *et al.* (2015) mapped smaller-scaled faults that follow the Loa River canyon which eroded and exposed the Chintoraste spring system (Fig. 1).

The Calama Basin is an extensional depocenter of Early Oligocene age. The basin fill consists of the Early Oligocene-Late Pliocene El Loa Group (May *et al.*, 2005; Tomlinson *et al.*, 2018). The El Loa Group includes alluvial and fluvial conglomerates, breccias, sandstones, siltstones, and limestones. Carbonate sediments are restricted to the Talabre Member of the Lasana Formation, and the Opache Formation. Talabre Member carbonates are expressed as thin (<60 cm-thick) beds of travertine and diagenetic cement, deposited between 13 and 10 Ma (Tomlinson *et al.*, 2018). The Opache Formation consists of lacustrine and palustrine limestones, sandy limestones, calcareous sandstones and conglomerates, travertines, and diatomites (May *et al.*, 2005; de Wet *et al.*, 2015, 2019; Tomlinson *et al.*, 2018). Opache Formation deposition ceased sometime after 3.37 Ma (May *et al.*, 2005). This time marks the largest extension of the Calama Basin, which is still active today but currently restricted to around the Chiu Chiu-Yalqui area (Tomlinson *et al.*, 2018).

3. Methods

3.1. Field work

Stratigraphic sections at El Sifón and Chintoraste were studied and measured over three field seasons. Samples (n=150) representative of the tufa lithologies were georeferenced and collected for analyses. Site locations were documented using global positioning system (GPS) methods. Local faults and fractures were measured and described.

3.2. Laboratory

3.2.1. Microscopy and diatoms

Hand samples and 80 thin sections, stained with potassium ferricyanide and Alizarin Red S (Dickson, 1966), were described. Photomicrographs were taken using a Leica DM EP microscope and ProgRes CF Jenoptik camera system. Subsamples for diatom analysis were dissolved twice in an acid bath of 10% HCl for 24 hours, rinsed with deionized water after each dissolution step, and filtered to remove any remaining carbonate. Processed samples were permanently mounted to slides using Norland Optical Adhesive NOA 61. Diatom frustules were identified using an Olympus BX53 microscope under 1000x magnification. Diatoms were recognized to species level using regional and cosmopolitan flora. Samples with abundant diatoms were enumerated to 300 valves per slide and counts were converted to percentages.

3.2.2. X-Ray Diffraction (XRD)

Fifteen tufa samples were powdered for X-Ray Diffraction (XRD) analysis to determine the polymorph of calcium carbonate present (Table 1). Samples were powdered using a Dremel Multipro 285 microdrill at low speed and run on a PANalytical X'Pert Pro PW3040 XRD spectrometer with Cu Kα radiation, with automated diffraction slit and a X'Celerator detector, using standard procedures, at Franklin & Marshall College.

3.2.3. Inductively Coupled Plasma-Optical Emission Spectroscopy (ICP-OES)

Eighty-two samples, representative of the range of field and petrographic carbonate morphologies, and referenced to the appropriate thin section, were drilled using a Dremel Multipro 285 microdrill at low speed to obtain 0.05 g for ICP-OES analysis of trace elements that commonly substitute for Ca and are routinely reported in carbonate geochemistry: Fe, Mg, Mn, and Sr. Samples were drilled under a magnifying glass to avoid siliciclastic contamination, dissolved in 10% HNO_3 and analyzed at Franklin & Marshall College on a SPECTROBLUE ICP-OES, with 750 mm focal length, a Paschen-Runge optical system, and 15 linear charge-coupled device array detectors. Calibrations were made to seven standards, diluted to appropriate concentrations, from Specpure commercial stock solutions referenced to known standards. The ICP-OES was calibrated before each run with a tuning solution to account for instrumental drift. Standard curves with 5+ points were compiled for each element with correlation coefficients >0.998. Standards JLs-1 and JDo-1 were run at the beginning and end of the run and were within <5% relative standard deviation (RSD) error of established values. Duplicate samples were within <1% RSD. Results are reported in parts per million (ppm) (Table 1).

3.2.4. Isotopes

Forty-eight samples, paired with material drilled for ICP, were powdered for C ($\delta^{13}C$) and O ($\delta^{18}O$) stable isotopes. Powders were run on a multi-prep device coupled to a Nu Instruments Optima Perspective dual inlet mass spectrometer at Rutgers University. Samples were reacted with 100% phosphoric acid at 90 °C for 13 minutes before transfer to the instrument. Values are reported relative to the Vienna Peedee Belemnite (V-PDB) (Table 1).

Strontium isotope ratios were measured from eleven carbonate samples leached with 1N HCl, as well as from water sampled from the modern Loa, Salado, and San Pedro rivers. Strontium was isolated from other elements using Sr-specific resin (Horwitz *et al.*, 1992) and analyzed using a Thermo Fisher Neptune Plus multicollector ICP-MS at Rutgers University (Table 2).

3.2.5. Radiometric dating

Two samples sent for U-Pb dating were collected at El Sifón from the outcrop on the northern side overlooking the Quebrada Turi, where the easternmost part of the Divisoco Fault System runs. One sample was near the exposure base, and the other was collected ~8 m higher, less than 2 m from the top surface. U-Pb dating was performed at SUNY-Stony Brook University in the laboratory of Dr T. Rasbury. After the samples were cleaned in distilled water and dried, they were weighed and a ^{205}Pb-^{236}U spike was added. The samples were dissolved in dilute nitric acid and placed on the hotplate overnight. The samples were dried down and then redissolved in 0.7 N HBr. U and Pb were isolated using a two-step anion exchange resin (Bio-Rad AG1-X8 100-200 mesh). Uranium was loaded on Re filaments with graphite and run as a metal on a Finnigan MAT 262 TIMS at between 1800-1900 °C. Lead was loaded on Re filaments with a silica gel (Gerstenberger and Haase, 1997) and run between 1300-1400 °C on a Finnigan MAT 262 TIMS. Ages were calculated using IsoplotR (Vermeesch, 2018), derived from the intercept with concordia on a Tera-Wasserburg plot. U-Pb data are shown in table 3.

4. Results

El Sifón (Fig. 2A) and Chintoraste (Fig. 2B) have laminated crystalline carbonate, brecciated limestone interbedded with sandstone or silty mudstone, botryoids, and stromatolites. The ratio of these facies is different between the two locations; detrital silty mudstone and sandy, stromatolitic, and crystalline calcite predominates at Chintoraste, whereas at El Sifón, aragonite botryoids, breccias, and thin sand to silt layers are interbedded with laminated aragonite.

TABLE 1. ICP-OES GEOCHEMICAL AND STABLE ISOTOPE RESULTS FOR CHINTORASTE AND EL SIFÓN OPACHE FORMATION TUFA LIMESTONE SAMPLES.

Chintoraste

Number	Latitude	Longitude	Fe (ppm)	Mg (ppm)	Mn (ppm)	Sr (ppm)	$\delta^{18}O_{V\text{-}PDB}$	$\delta^{13}C_{V\text{-}PDB}$
CT1 22	-22.52088	-69.06266	46.95	898.89	46.88	2,274	0.48	3.07
CT1 22A	-22.52088	-69.06266	42.81	470.37	53.23	3,347.52	2.87	3.08
CT2 22-1	-22.51993	-69.06341	352.27	153.97	53.85	3,077.92	-5.33	3.2
CT2 22-2	-22.51993	-69.06341	336.36	166.67	55.38	3,411.33	-5.85	3.37
CT2 22-3	-22.51993	-69.06341	243.18	2,460	67.69	1,629.48	-0.85	2.38
CT2 22-4	-22.51993	-69.06341	140.11	1,561	229.11	581.98	-5.44	2.97
CT3 22A	-22.51993	-69.06341	216.59	553.15	139.75	435.33	-5.01	0.67
CT3 22B	-22.51993	-69.06341	178.08	1,932	256.86	432.37	0.74	2.44
CT4 22	-22.51967	-69.06386	308.55	1,265	416.23	539.34	-4.03	7.25
CT4 22A	-22.51967	-69.06386	742.99	1,265	661.16	514.85	-5.04	6.11
CT4 22B	-22.51967	-69.06386	1,376	1,265	591.74	494.44	-4.62	7
CT4 22D	-22.51967	-69.06386	457.65	1,265	476.73	364.97	-4.85	3.8
CT7 22	-22.51967	-69.06386	115.23	1,265	39.42	500.11	-6.27	2.69
CT9 22-1	-22.51893	-69.06378	129.9	1,265	82.81	1,071.11	-6.04	2.09
CT9 22-2	-22.51893	-69.06378	1546	1,265	819.28	571.16	-5.19	4.35
CT10 22	-22.51953	-69.06418	859.17	1,265	865.3	2,648.88	-5.82	2.3
CT14 22A	-22.51978	-69.06379	40.19	1,265	57.56	2,169.69	-5.05	2.46
CT14 22B	-22.51978	-69.06379	47.86	1,265	42.6	3,631.21	-4.24	3.14
CT15 22	-22.51978	-69.06379	3678	1,265	1,703	369.28	-4.75	2.11
CT18 22A	-22.51993	-69.06342	1033	1,265	850.3	426.76	-4.81	6.07
CT18 22B	-22.51993	-69.06342	2229	1,265	382.97	355.97	-4.17	2.71
CT18 22C	-22.51993	-69.06342	no data	1,265	320.88	438.56	-3.07	3.1
CT19 22A	-22.51988	-69.06349	no data	1,265	119.45	3,373.91	-4.89	2.77
CTO 2-22	-22.51982	-69.06378	no data	1,265	34.63	126.19	no data	no data
CTO 5	-22.51982	-69.06378	no data	1,265	222.74	314.24	-5.11	3.46
CTO rd	-22.52031	-69.06342	no data	1,265	1,117.74	1,312.67	-5.21	-1.72
CTO wh	-22.52031	-69.06342	1,341	1,265	943	260.2	no data	no data
CTO2 22	-22.51880	-69.06370	9,005	1,265	2,462	233.5	no data	no data
WCSL 3	-22.52037	-69.06419	7,890	1,265	2,307	249.2	no data	no data
WCSL 4	-22.52112	-69.06238	1,320	1,265	778.7	382.2	no data	no data
CT-39-12-A	-22.51978	-69.06379	6,090	1,265	3,397	291	no data	no data
CT-39-12-B	-22.51978	-69.06379	669.4	1,265	64.8	2,814	no data	no data
CT-39-12-C	-22.51978	-69.06379	332.8	1,265	31	1,387	no data	no data
CT-39-12-D	-22.51978	-69.06379	117.5	1,265	41.1	2,933	no data	no data
CT-39-12-E	-22.51978	-69.06379	285.1	1,265	59.5	1,265	no data	no data
CT-46-12-C*	-22.51993	-69.06342	127.1	1,265	42.2	981	no data	no data
CT-46-12-E^	-22.51993	-69.06342	124.1	1,265	35.6	3,656	no data	no data
CT-46-12-G*	-22.51993	-69.06342	117.5	1,265	41.1	2,933	no data	no data
CT-46-12-I^	-22.51993	-69.06342	285.1	1,265	59.5	1,265	no data	no data
CT-46-12-K^	-22.51993	-69.06342	127.1	1,265	42.2	981	no data	no data
CT-46-12-M*	-22.51993	-69.06342	124.1	1,265	35.6	3,656	no data	no data
CT-46-12-O#	-22.51993	-69.06342	511	1,265	161.5	1,824	no data	no data
Count			37	42	42	42	29	29
Average			1178.12	1,267.66	482.79	1,423.96	-3.74	3.21

table 1 continued.

El Sifón

Number	Latitude	Longitude	Fe (ppm)	Mg (ppm)	Mn (ppm)	Sr (ppm)	$\delta^{18}O_{\text{V-PDB}}$	$\delta^{13}C_{\text{V-PDB}}$
EL+B77S 5	-22.28261	-68.37584	no data	590.01	12.55	9,989.1	-3.6	6.23
ELS B+2M	-22.28255	-68.37578	259.04	51.42	13.04	16,981.73	-4.67	7.64
ELS6 +8M	-22.28268	-68.37592	390.63	267.46	3.38	11,052.28	-5.23	8.52
ELS6 BASE	-22.28268	-68.37592	187.5	142.86	0.88	15,516.3	-5.78	6.9
ES2 22	-22.28268	-68.37592	178.13	157.5	1.03	16,151.66	-5.57	6.9
ES3 22	-22.27970	-68.37764	146.88	65.87	0.03	24,036.67	-4.87	7.19
ES4 22-1	-22.27970	-68.37764	146.88	16.06	11.38	21,148.42	-4.8	6.94
ES4 22-2	-22.27970	-68.37764	48.85	57.83	12	19,527.1	-4.47	7.69
ES4 22-3	-22.28092	-68.37411	0	18.26	10.07	24,710.15	-4.76	6.2
ES5 22-1	-22.28438	-68.37236	118.97	42.15	17.77	19,742.95	-3.86	7.64
ES5 22-2	-22.28438	-68.37236	624.64	52.59	21.32	16,268.78	-4.36	7.64
ES5 22-3	-22.28438	-68.37236	29.9	97.82	15.55	24,900.86	-4.52	7.31
ES8 22	-22.28438	-68.37236	305.82	245.9	20.14	16,640.55	-3.56	6.95
ES11 22	-22.28438	-68.37236	0	94.36	19.71	12,102.68	-3.51	7.39
ES11A 22-1	-22.31740	-68.41699	0	534.91	3.45	15,797.69	-1.28	6.14
ES11A 22-2	-22.28504	-68.37612	23.4	1191	5.5	15,442	no data	no data
ES11A 22-3	-22.28504	-68.37612	36.7	505	78.4	12,649	no data	no data
ES13 22	-22.28504	-68.37612	40	645	19.3	13,096	no data	no data
SOPT 2	-22.28504	-68.37612	13.9	103.6	5.5	18,085	no data	no data
O-65-A-SR	-22.28504	-68.37612	14	153.8	5.5	15,274	no data	no data
O-65-B-SR	-22.28504	-68.37612	5.5	278	5.5	16,712	no data	no data
O-65-C-SR	-22.28504	-68.37612	10.5	97.2	5.5	17,922	no data	no data
O-65-D-SR	-22.28504	-68.37612	16.8	168	5.5	17,697	no data	no data
O-65-E-SR	-22.28504	-68.37612	6	123.6	5.5	14,308	no data	no data
O-65-F-SR	-22.28504	-68.37612	9.5	127.7	5.5	16,136	no data	no data
O-65-G-SR	-22.28504	-68.37612	13.8	158.7	5.5	17,297	no data	no data
O-65-H-SR	-22.28504	-68.37612	14.8	104.7	5.5	18,521	no data	no data
O-65-I-SR	-22.28504	-68.37612	46.5	76.0	5.5	18,845	no data	no data
O-65-J-SR	-22.28268	-68.37592	0	254.2	3.3	6,443	no data	no data
O-65-K-SR	-22.28268	-68.27592	0	234.7	0	6,453	no data	no data
O-65-L-SR	-22.28268	-68.27592	7.3	247.9	49.4	6,461	no data	no data
O-65-M-SR	-22.28268	-68.27592	2.4	278.3	6.3	6,462	no data	no data
O-31-12-H*	-22.28268	-68.27592	60.2	349.9	11.1	6,462	no data	no data
O-31-12-G*	-22.28268	-68.27592	1.6	484.1	17	6,485	no data	no data
O-31-12-F*	-22.28268	-68.27592	0	333.4	20.8	6,459	no data	no data
O-31-12-E*	-22.28268	-68.27592	31.9	408.2	6.3	6,459	no data	no data
O-31-12-D*	-22.28268	-68.27592	60.2	349.9	11.1	6,462	no data	no data
O-31-12-C*	-22.28268	-68.27592	1.6	484.1	17.0	6,485	no data	no data
O-31-12-B*	-22.28268	-68.27592	0	333.4	20.8	6,459	no data	no data
O-31-12-A*	-22.28268	-68.27592	31.9	408.2	6.3	6,459	no data	no data
Count			35	40	40	40	19	19
Average			79.77	324.19	11.87	14,870.51	-4.30	7.02

“0.0” values indicate below detection limit. Count refers to the total number of samples for each location, grouped by element and isotope. XRD results for several samples are given as: * = aragonite with minor calcite; ^ = calcite; and # = calcite with minor aragonite.

TABLE 2. STRONTIUM ISOTOPE DATA FOR CHINTORASTE AND EL SIFÓN OPACHE FORMATION TUFA LIMESTONE SAMPLES.

Sample	Latitude (°)	Longitude (°)	^{87}Sr/^{86}Sr	2σ
El Sifón				
ES4 22	-22.28268	-68.37592	0.707639	0.000014
ES8 22	-22.28092	-68.37411	0.707459	0.000010
AIQ 5	-22.28451	-68.37244	0.707850	0.000010
ELS6 BASE	-22.28504	-68.37612	0.707600	0.000016
ELS6 +8M	-22.28504	-68.37612	0.707860	0.000018
Chintoraste				
CT10 22	-22.51953	-69.06418	0.706596	0.000020
CT4 22	-22.51967	-69.06386	0.706714	0.000016
CT7 22	-22.51967	-69.06386	0.706588	0.000016
WCSL 1 Red	-22.52031	-69.06342	0.706731	0.000014
WCSL 1 White	-22.52031	-69.06342	0.706505	0.000014
WCSL 4	-22.52112	-69.06238	0.706940	0.000014
El Sifón (average ^{87}Sr/^{86}Sr)	0.707682			
El Sifón ^{87}Sr/^{86}Sr (standard deviation)"	0.000172			
Chintoraste (average ^{87}Sr/^{86}Sr)	0.706679			
Chintoraste ^{87}Sr/^{86}Sr (standard deviation)"	0.000153			

TABLE 3. U-PB DATA USED TO DETERMINE AGE OF THE EL SIFÓN TUFA.

Sample	U (ppm)	2σ (%)	Pb (ppm)	2σ (%)	^{238}U/ ^{204}Pb	2σ (%)	^{206}Pb/ ^{204}Pb	2σ (%)	^{238}U/ ^{206}Pb	2σ (%)	^{207}Pb/ ^{206}Pb	2σ (%)
El Sifón, ~8 m above base												
LG8-1	23.82	0.09	0.22	3.43	7817.21	5.50	26.89	1.46	290.7	5.7	0.5955	2.5524
LG8-2	22.86	0.10	0.19	3.50	8600.54	5.66	27.77	1.59	309.7	5.9	0.5779	2.8259
LG8-3	21.37	0.11	0.18	3.80	8531.39	6.20	27.65	1.74	308.5	6.4	0.5811	3.1066
LG8-4	22.80	0.14	0.26	4.21	6157.08	5.52	25.64	2.93	240.1	6.2	0.6287	6.4029
LG8-5	21.71	0.10	0.45	4.38	3268.83	4.65	22.08	3.65	148.0	5.9	0.7299	7.0717
age=7.12±0.51 (2σ) Ma												
El Sifón, base												
LGB-1	17.29	0.09	0.27	2.51	4336.96	3.68	23.67	0.81	183.2	3.8	0.6697	1.4121
LGB-2	12.30	0.07	0.27	2.98	3020.35	4.23	22.03	1.26	137.1	4.4	0.7211	2.3565
LGB-3	15.32	0.08	0.21	3.22	5010.93	4.90	24.06	1.30	208.2	5.1	0.6612	2.4290
LGB-4	8.90	0.07	0.25	2.40	2295.52	3.01	21.03	0.54	109.1	3.1	0.7443	1.1177
LGB-5	11.93	0.07	0.23	2.95	3399.33	4.42	22.17	0.73	153.3	4.5	0.7112	1.1600
LGB-6	17.37	0.07	0.19	3.52	6154.28	5.64	25.13	1.25	244.9	5.8	0.6316	2.0515
age=6.93±0.62 (2σ) Ma												

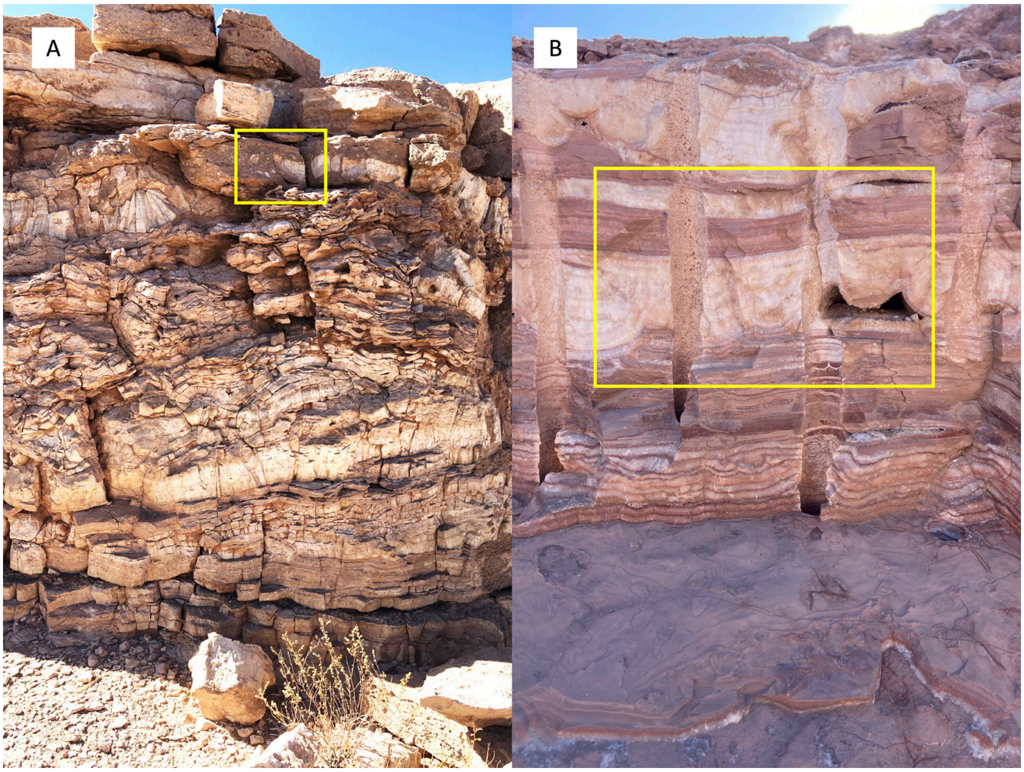

FIG. 2. Field photographs of the two springs. **A.** El Sifón tufa showing layered tufa overlain by a horizon of botryoidal aragonite, partially brecciated. This is part of the outcrop shown in figure 4B. For scale, the plants at base are ~15 cm tall. Boxed area refers to figure 8A. **B.** Chintoraste tufa composed of laminated calcite and interbedded red silt and claystone, overlain by thick horizons of botryoidal aragonite. Rounded vertical pipes in the photograph are drill holes (3 cm diameter) made when this part of the tufa was mined by local artisans. Boxed area refers to figure 12A.

4.1. El Sifón

The Quebrada Turi canyon bisects the Opache Formation at the El Sifón location (Fig. 3), exposing the underlying Sifón Ignimbrite (Fig. 4A). Laminated tufa forms a mound atop sandy brecciated horizons, which overlay additional laminated tufa (Fig. 4B). Uranium concentrations at El Sifón range from 8.9 to 23.8 ppm, and Pb between 0.18 and 0.45 ppm. U is higher in the upper bed than near the base, while Pb is evenly distributed. The U/Pb ratios range between 35 and 121. The ages are derived from the intercept with concordia on a Tera-Wasserburg plot using the sub-samples for each hand sample. Statistically they are within error of each other, the sample from the base yielding an age of 6.93±0.62 (2σ) Ma and the sample 8 m above it an age of 7.12±0.51 (2σ) Ma. These ages indicate the rapidity of carbonate deposition, but lack the precision to more accurately distinguish the age difference. The contact between the Sifón Ignimbrite and the Opache Formation is dominated by gravel composed of *in situ* weathered ignimbrite, which is itself overlain by detrital sands and gravels, followed by laminated limestone (Fig. 5). Limestone thickens and thins across the undulating upper surface of the ignimbrite (Fig. 6).

The Divisoco Fault System offsets Opache Formation strata with dextral slip (Álvarez *et al.*, 2023). On the north side of Quebrada Turi, the fault's strike was ~150°, and a near vertical dip. The downthrown side is to the southwest, with ~6 m vertical displacement. Tufa limestone is thicker at the fault's break in slope (Fig. 5). Small aragonite-lined fractures cut the Opache Formation, some with associated tufa intraclasts, detrital sands, and ignimbrite fragments within them. They are subvertical, with no consistent strike, implying substrate instability on the fault-related slope.

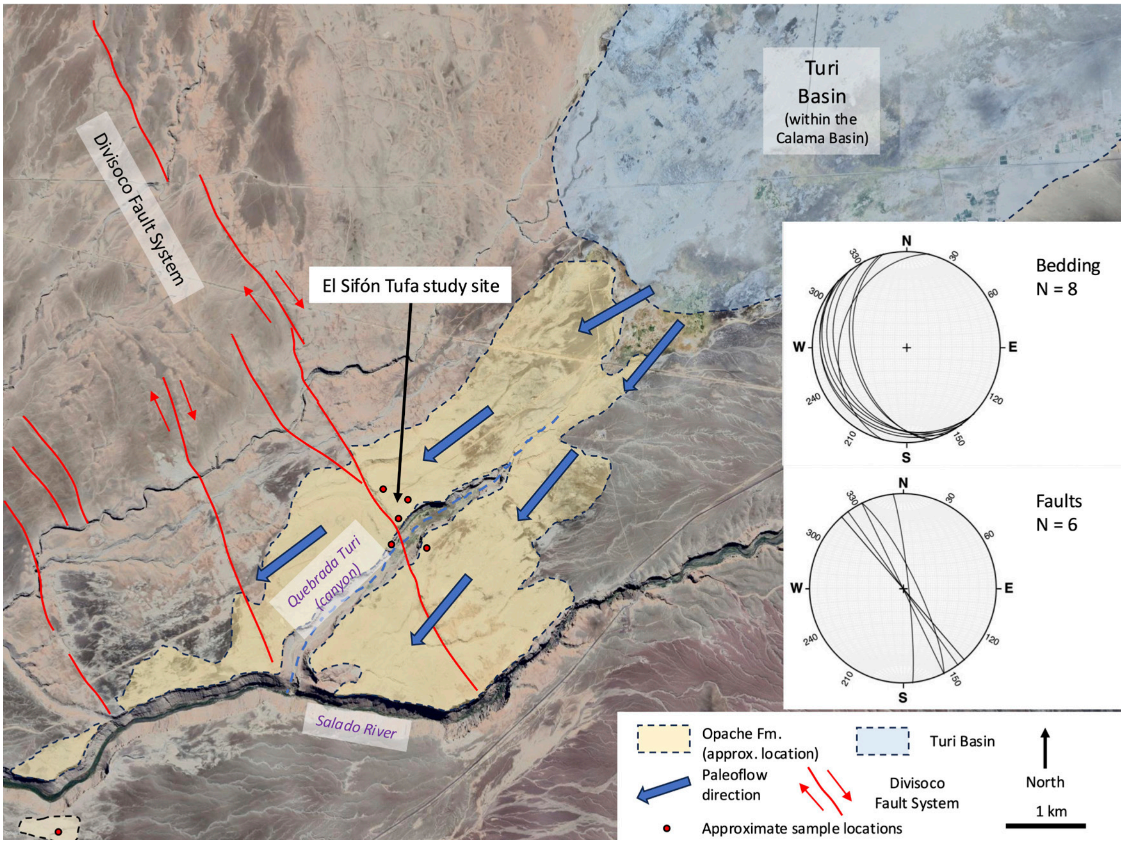

FIG. 3. El Sifón study site. The tufa is located adjacent to the Turi Basin to the northeast and the Salado River to the south. Tufa facies were sampled in detail where the Quebrada Turi canyon bisects the deposit. The Divisoco Fault System is a prominent feature in the landscape. Strike and dip of bedding and minor faults are plotted on stereonets. The sampling sites are shown as red circles. Image from Google Earth, 2025 Airbus.

Bedding dips gently about 0.5° degrees to the southwest, corresponding to the current topographic surface; however, at the fault zone, the topographic slope is ~11° and bedding dips as steeply as 45° on the south side of the canyon. The Opache Formation tufa limestone tapers to zero thickness southeast and northwest of this site and is partly eroded by the modern Salado River to the southwest (Fig. 3).

Bedding within the El Sifón tufa consists of brecciated beds, thin micrite layers, and >1 m thick successions of laminated and layered crystalline aragonite (Fig. 2A). Crystalline aragonite layers range from flat-lying, bedding parallel, to complexly convoluted, and vary in color from white to pale green. Interbedded sands and silts are generally brown and grey, although some have a pale red color (Fig. 7). Clasts of broken tufa are admixed with igneous rock fragments, angular to subrounded detrital sand grains, and micritic intraclasts in sand and gravel beds (Fig. 8). Millimeter- to cm-scale cavities, either unfilled or containing botryoids, crystal linings, and/or fine sediment, also occur (Fig. 7). Typically, the cavities are bedding parallel, form distinct horizons, and have relatively flat floors. There is a paucity of stromatolite forms, but where present, they are mm-thick crinkly laminations or mm-size domes.

The dominant polymorph at the El Sifón site is aragonite, with some minor calcite (Table 1). ICP-OES results show that the aragonite is highly enriched in Sr (up to 24,901 ppm; Table 1). Aragonite's propensity to accommodate the relatively large Sr ion is expected because of its crystal structure,

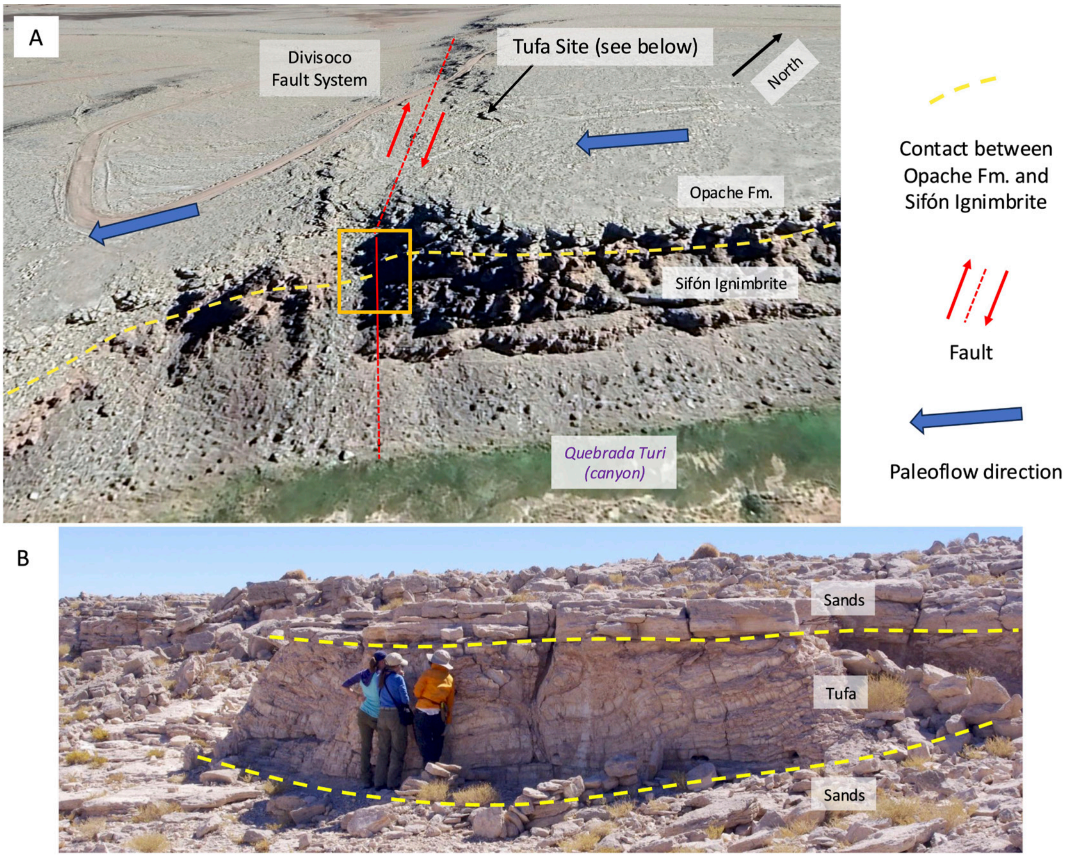

FIG. 4. Field relations at El Sifón. **A.** View of the El Sifón study site looking northwest across the Quebrada Turi canyon. Paleoflow direction is to the southwest. The Opache Formation overlies the Sifón Ignimbrite, and the transtensional Divisoco Fault System marks a prominent break in slope. Yellow square refers to figure 5. Image from GoogleEarth, 2025 Airbus. **B.** Field photograph of a ~2 m thick tufa mound marked in panel A as Tufa Site. Sandy horizons underlie and overlie the tufa. Middle person in photograph is ~1.5 m tall for scale.

relative to calcite, thus aragonite typically contains higher Sr^{2+} concentrations than calcite (Veizer, 1983). Present day waters in the Turi Basin have Sr and Mg concentrations that do not exceed 5.2 and 54 ppm, respectively (Romero *et al.*, 2003; Godfrey *et al.*, 2019), so the El Sifón tufa high Sr (average 14,871 ppm) and magnesium (average 324 ppm) values are unusual (Table 1).

Petrographic features include acicular aragonite crystals as laminations and fans, alternations in light and dark microbial laminations, and mud drapes over aragonite crystals (Fig. 9). Pyrolusite occurs as fine dendrites within the carbonate laminae and is widespread on the Opache Formation's uppermost surface. Calcite, where present, stains as non-ferroan (Dickson, 1966). Aragonite crystals may have sharp crystal boundaries (Fig. 9B), or, less commonly, have micritic microborings and/or serrated margins (Fig. 9C), indicating microbial infestation and/or incipient dissolution.

Diatom valves were absent or sparse in most samples. The exception to this is an upper-most sample from the El Sifón location (sample ES 13-22), where abundant (>5%) diatoms include *Nitzschia inconspicua* Grunow (50%), *Planothidium delicatulum* Cleve and Grunow (31%), and *Staurosirella pinnata* (Ehrenberg) D.M. Williams and Round (15%) (Fig. 10). Other samples from the El Sifón tufa that contain <5% diatoms are consistent with the same species assemblage above.

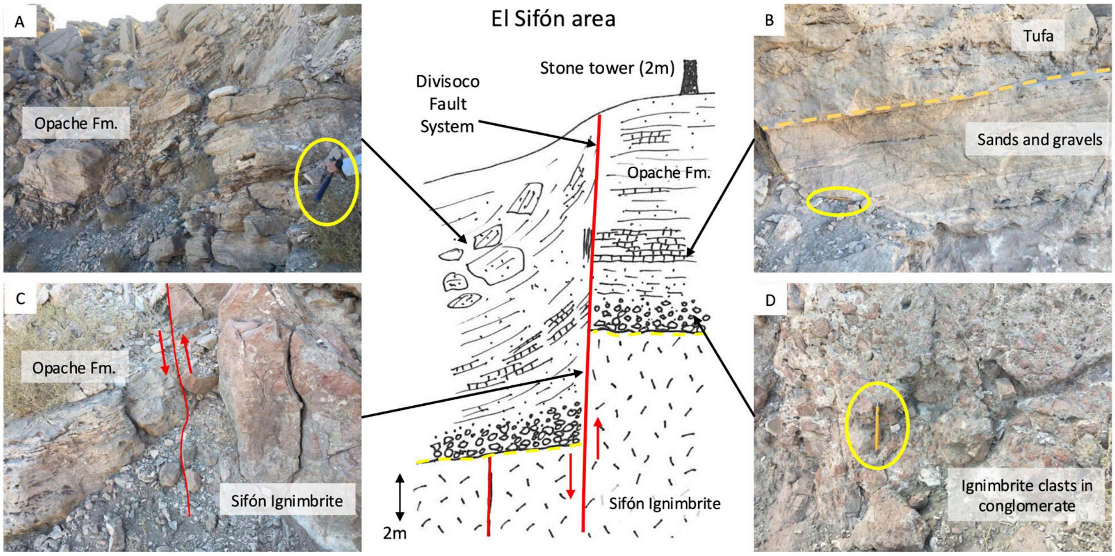

FIG. 5. Details of the layered Opache Formation at El Sifón. This is a closer view of the boxed area in figure 4A. **A.** The upper left part of the photograph shows slabs of angled tufa on the downthrown side of the fault. Tufa on the right side is relatively flat-lying. Hammer (circled) is 33 cm long. **B.** Interbedded detrital sands and gravels overlain by porous layered tufa. Pencil (circled) is 15 cm long. **C.** Trace of one of the faults of the transtensional Divisoco Fault System that offsets both the Sifón Ignimbrite and Opache Formation strata. Field of view is 2 m. **D.** The uppermost surface of the ignimbrite showing at least partially *in situ* weathered ignimbrite gravels with carbonate cement. Pencil (circled) is 15 cm long. The sketch of the field relations shows the Opache Formation and Sifón Ignimbrite on either side of the fault for context.

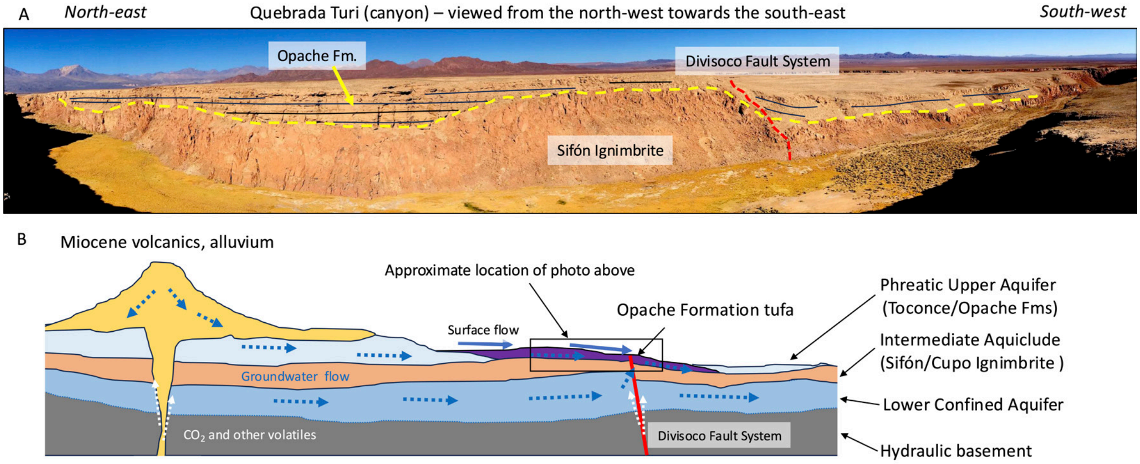

FIG. 6. **A.** Panoramic field photograph at El Sifón showing the undulating surface of the Sifón Ignimbrite in contact with the overlying Opache Formation. View is to the ESE. **B.** Sketch of the area with subsurface geology and groundwater flow paths, interpreted from regional topography, Houston (2007), and Jordan *et al.* (2015).

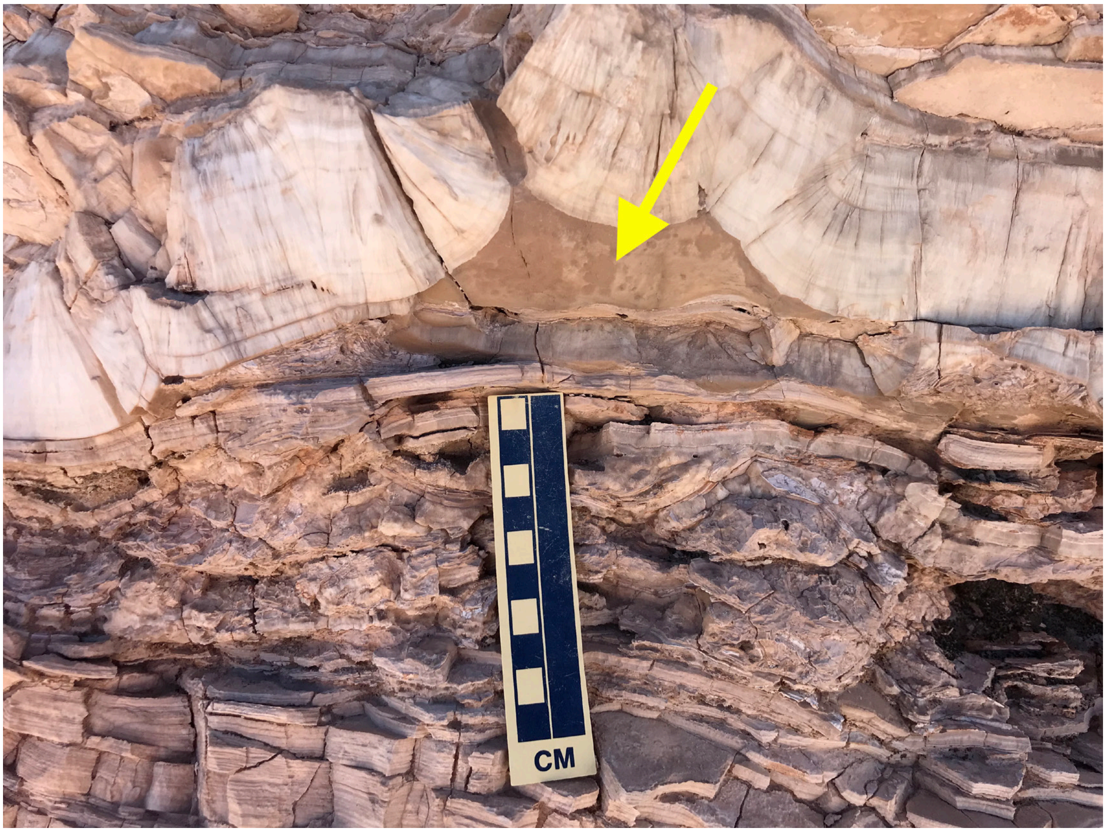

FIG. 7. *In situ* aragonite botryoids above thinly bedded and disrupted tufa horizons at El Sifón. The cavity the botryoids grew into is occluded with red silty mudstone (arrow). This field photograph is a close-up of the upper mound bed shown in figure 4B and is laterally equivalent to the boxed horizon in figure 2A.

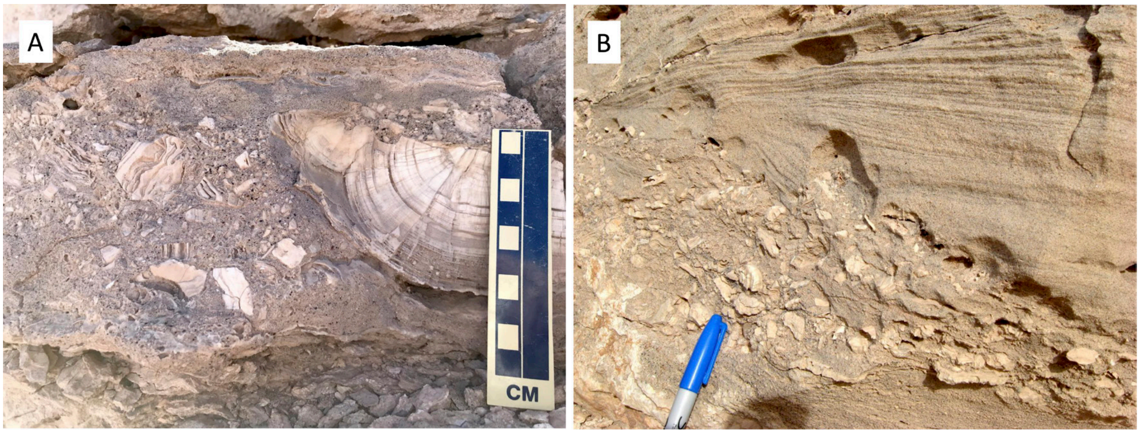

FIG. 8. Tufa-sand breccia at El Sifón. **A.** Large botryoid clast admixed with poorly sorted angular tufa fragments in a detrital sand matrix. This is a closer view of the boxed area in figure 2A. **B.** Tufa breccia in a sand matrix, overlain by cross-bedded sands in a shallow channel near the top of the tufa complex. Pen cap is 5 cm long.

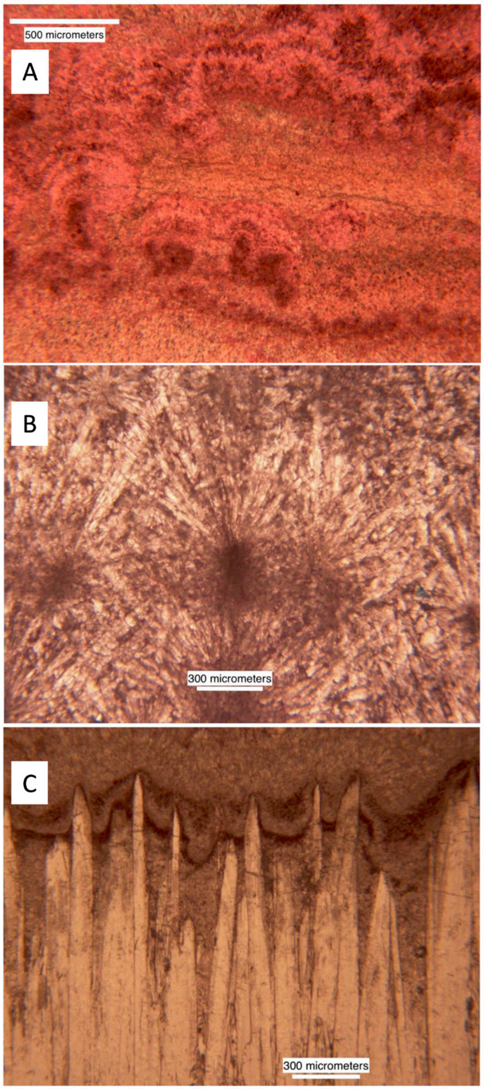

FIG. 9. Stained thin sections from El Sifón. **A.** Multiple generations of microstromatolites (dark microbial shrub growths and laminations), within aragonite crystal spar. **B.** Petrographic view of microbotryoids composed of organic-rich nuclei and radiating aragonite crystals. **C.** Slender aragonite crystals with both sharp and corroded crystal faces draped by detrital muds and silts.

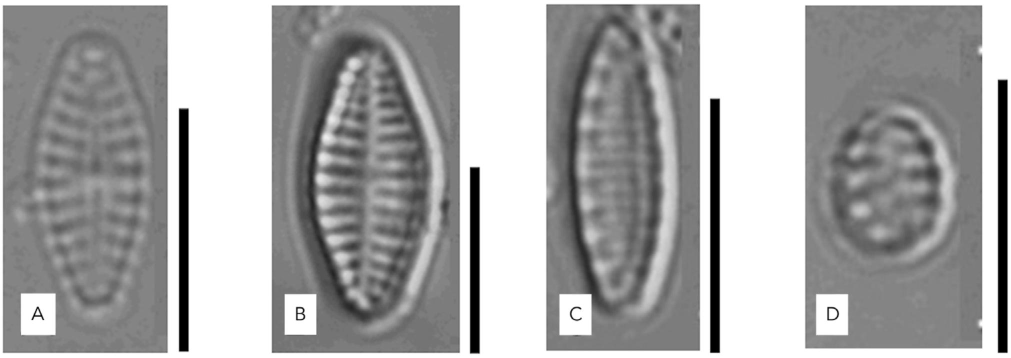

FIG. 10. Dominant species of diatoms from El Sifón. **A-B.** *Planothidium delicatulum* Cleve and Grunow. **C.** *Nitzschia inconspicua* Grunow. **D.** *Staurosirella pinnata* (Ehrenberg) D.M. Williams and Round. The scale bars are 5 microns each.

4.2. Chintoraste

Opache Formation tufa at the Chintoraste location consists of three fissure ridges. The tufas are ~50 m apart and ~20 m thick (Fig. 11). Erosion by the Loa River exposed the Chintoraste spring system carbonates. Carbonate-rich veins within the fissure ridges, up to 4 m wide, are lined with multiple generations of calcite and lead into the tufa deposit (Fig. 11C, D). The veins are oriented NNE-SSW and are steeply dipping.

In the northern part of the tufa deposit, bedding has variable dips, averaging 45° to the ESE, while in the southern and central parts of the deposit bedding planes are flatter, dipping generally NNW (Fig. 11A).

The tufas consist of meter-thick, layered to laminated crystalline carbonate (Fig. 12A), interbedded with red silty mudstone, and cm-scale oncolites and stromatolites (Fig. 12B). Intercalated porous tufa micrite and possible plant fossils and stem molds (C. Williams, personal communication, 2020) are also present. Microterracettes, or cm-scale, stepwise carbonate layers with curved, near-vertical fronts occur in small areas (<1 m across) down the surface of the carbonate ridges, indicating water flow away from the fissures (Fig. 13A). Ripple marks and flowstone, or smooth limestone in shallow channels, are present on the ridge surfaces (Fig. 13B) and are now subhorizontal, indicating ongoing tectonics.

Petrographically, the Chintoraste tufa consists of equant to dog-toothed calcite interlayered with microstromatolites (Fig. 14A, B), cm- to mm-scale oncolites, pore-lining spar, and calcite cement around detrital grains. Calcite crystals generally stain non-ferroan (Dickson, 1966), although ferroan calcite is present as fine-scale alternations with non-ferroan calcite, or as late-stage void filling cement in some samples. Pyrolusite occurs as fine dendrites within the carbonate laminae. Acicular aragonite crystal laminations occur within the calcite layers but particularly form large crystal fans or botryoids within cavities (Figs. 2B and 12A) and consist of fan shaped crystal arrays with sweeping extinction (Fig. 14C). Fine-grained red mudstone drapes over crystal terminations, fills, or partially fills cavities, and forms discreet red and clear alternating mud and crystal laminations (Fig. 14A). Oncolites are present as <1 cm-thick lenses and may coalesce into stromatolite laminations across their upper surfaces. Microdigitate stromatolites widen from their base to their upper surfaces and are interbedded with crystalline calcite layers or clotted carbonate, frequently terminating in horizons of detrital sand and mud (Figs. 12B and 14B). Light-colored crystalline and dark micritic alternations define the oncolite and stromatolite layered fabric (Fig. 14B). Diatom valves are absent or sparse in most samples, but where present, consist of an assemblage of *Nitzschia inconspicua*, *Planothidium delicatulum*, and *Staurosirella pinnata*.

Breccias, consisting of fragments of laminated carbonate tufa in red silty mudstone, and intraclast-rich, volcanic detrital sands, occur in lenses and cm-thick beds at the Chintoraste site. Millimeter to cm-scale cavities, typically with flat floors and irregular upper surfaces, may be unfilled, or occluded by large aragonite botryoids and crystal fans (Figs. 2B and 12A). Acicular aragonite was converted to non-ferroan calcite locally, particularly in association with fractures (Fig. 14D).

Transitions between laminated crystalline calcite horizons, stromatolite-rich beds, and calcite-cemented sands occur over short distances both laterally and vertically. For example, a 30 cm thick vertical succession shows a transition from purely acicular aragonite to aragonite with minor calcite, overlain by a microstromatolite and micritic-rich fabric, to a layer of detrital sands and diatoms. Similar changes occur laterally within a few meters lateral distance.

The dominant polymorph at the Chintoraste location is calcite, with lesser high-Mg calcite and aragonite (Table 1). Chintoraste samples show higher concentrations of Mn^{2+} (average 483 ppm), Mg^{2+} (average 1,268 ppm), and Fe^{2+} (average 1,178 ppm), but lower Sr^{2+} values (average 1,424 ppm) than those from the El Sifón site (Fig. 15; Table 1).

4.3. Isotope geochemistry

The oxygen and carbon stable isotope composition of carbonate from both spring sites exhibit considerable overlap in values, but there are important differences (Fig. 16). Samples from both spring sites form a cluster at high $\delta^{13}C$ and intermediate $\delta^{18}O$, with more samples from El Sifón plotting in a high $\delta^{13}C$ group, and samples from Chintoraste showing less change in $\delta^{13}C$, but considerable variation

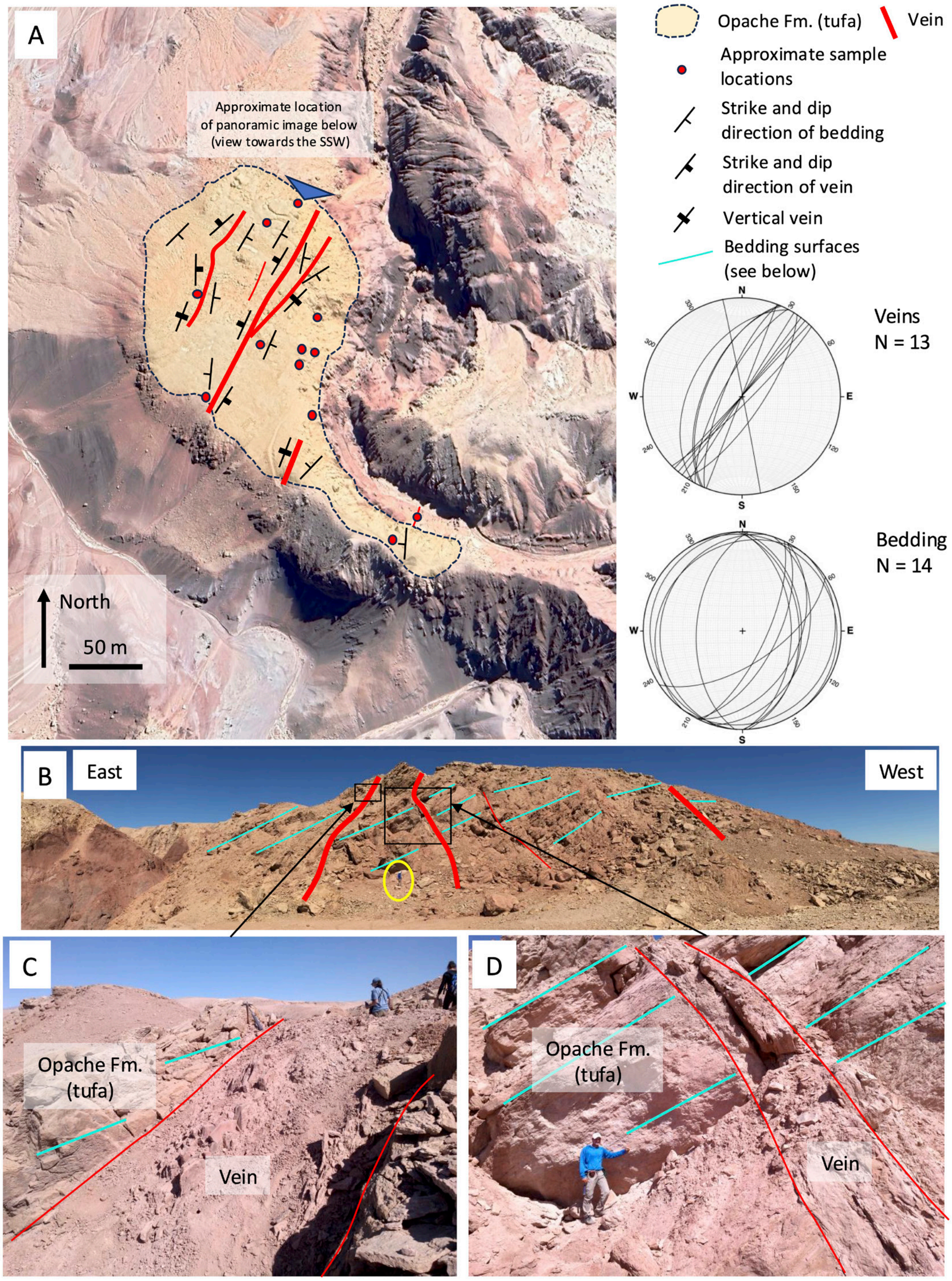

FIG. 11. Chintoraste study site. **A.** Distribution of layered tufa, veins, and the strike and dip of bedding and veins. The sampling sites are shown as red circles. Image from Google Earth, 2025 Airbus. **B.** Panoramic field photograph looking to the SSW (see blue arrowhead in panel A for location), showing orientation of major veins and bedding. Person for scale, circled, is ~1.8 m tall. **C.** Carbonate-filled vein oblique to tufa bedding (see box in panel B for location, arrowed). Seated person for scale is ~1.5 m high. **D.** Prominent carbonate-filled vein and dipping tufa strata (see box in panel B for location, arrowed). Person is ~1.8 m tall.

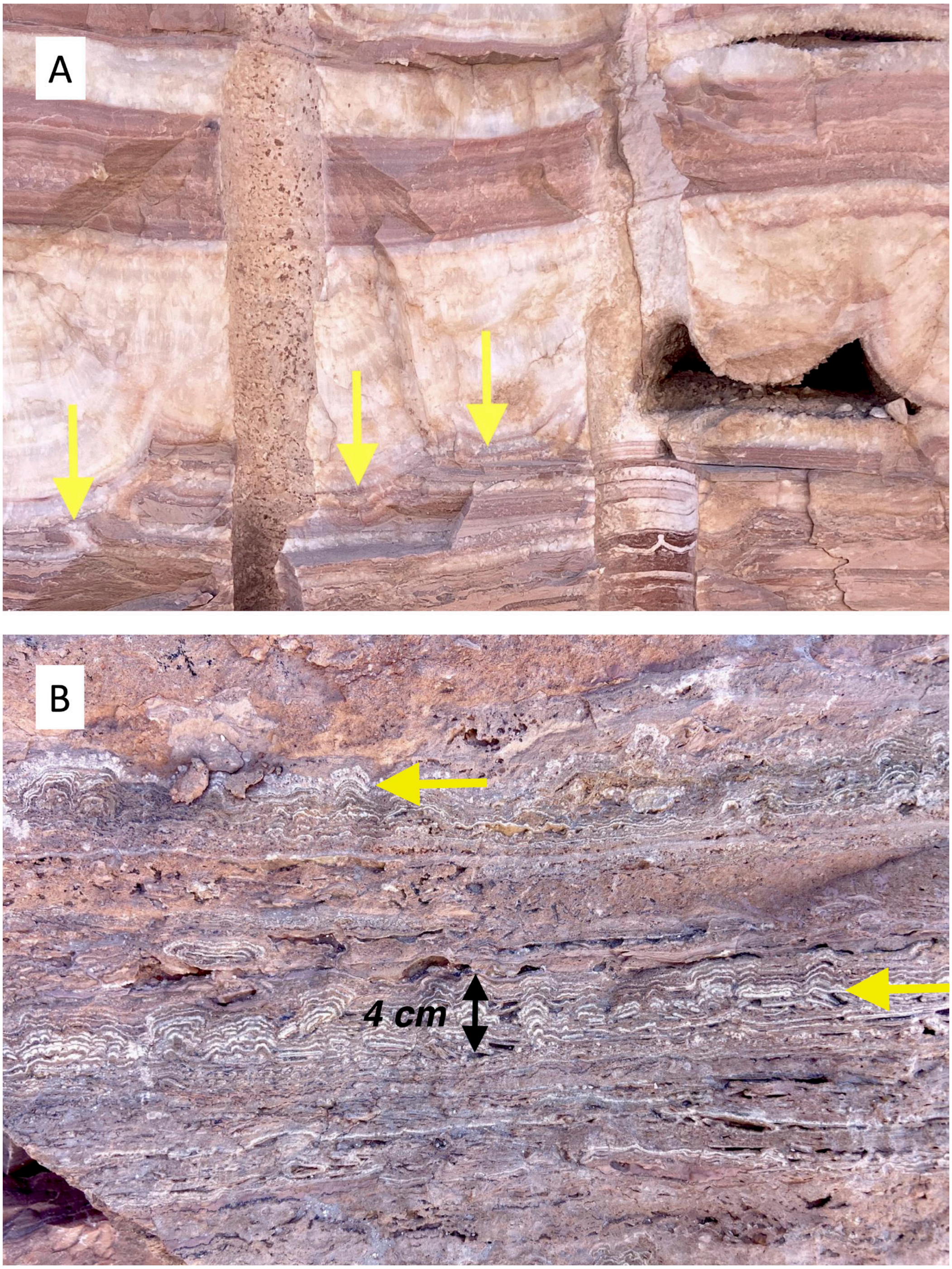

FIG. 12. Large botryoids and small stromatolites at Chintoraste. **A.** Field photograph of aragonite botryoids that grew into an open cavity, but also impinged on the tufa and mud layers below (yellow arrows), disrupting laminations that must have been semi-plastic during botryoidal development. This is a closer view of the boxed area in figure 2B. Drill holes are 3 cm diameter. **B.** Field photograph of stromatolite horizons interbedded with porous tufa layers. Yellow arrows indicate stromatolite-rich horizons. Black arrow shows large stromatolites that are 4 cm in vertical height.

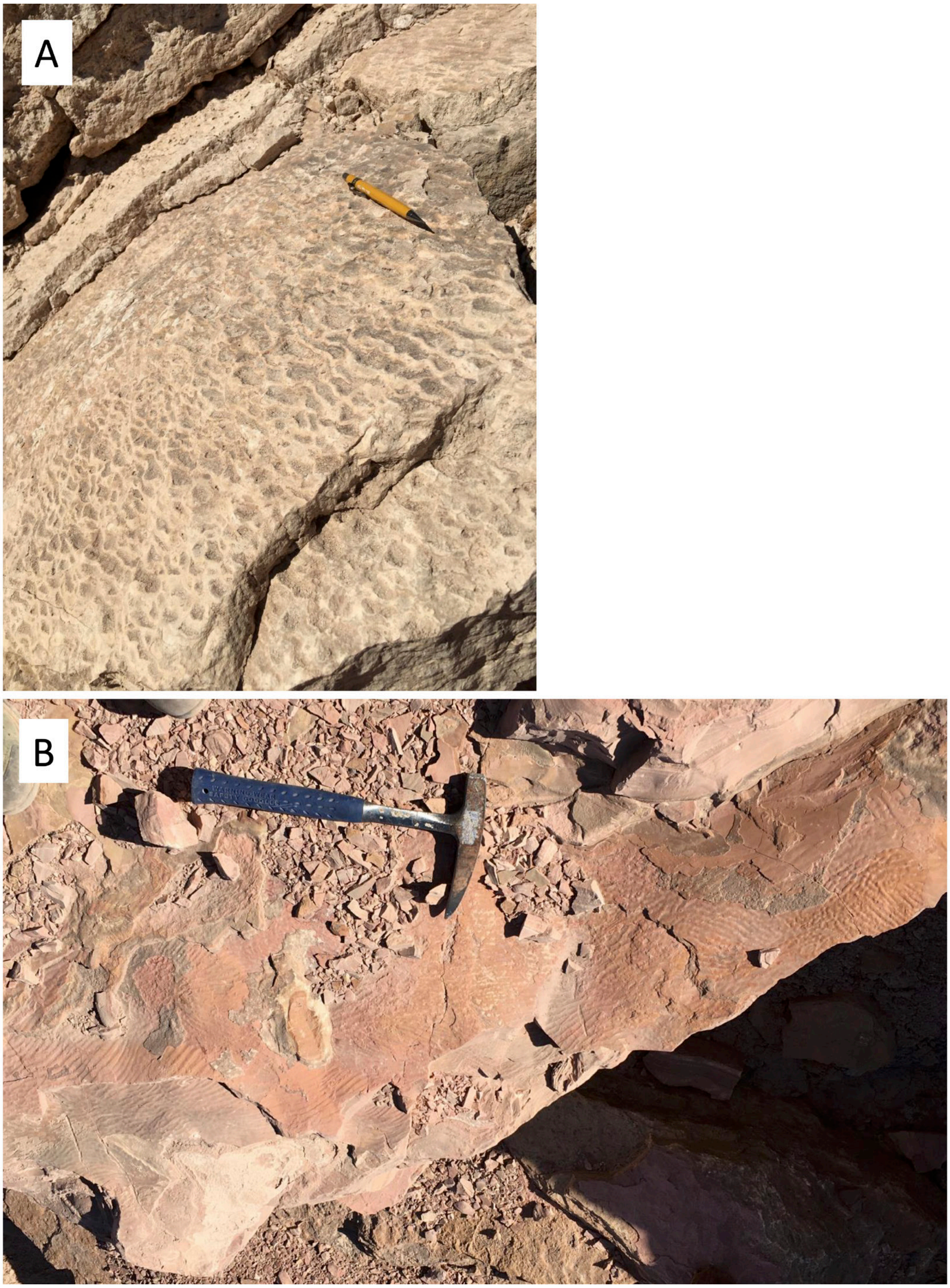

FIG. 13. Field evidence for tufa water flowing from vein/fissure sources at Chintoraste. **A.** Stepped microterracettes developed on a bedding plane, indicating water flow downslope away from the vein. Pencil is 15 cm long. **B.** Ripple marks on multiple bedding planes, indicating shallow water flow sourced from vein. Hammer is 33 cm long.

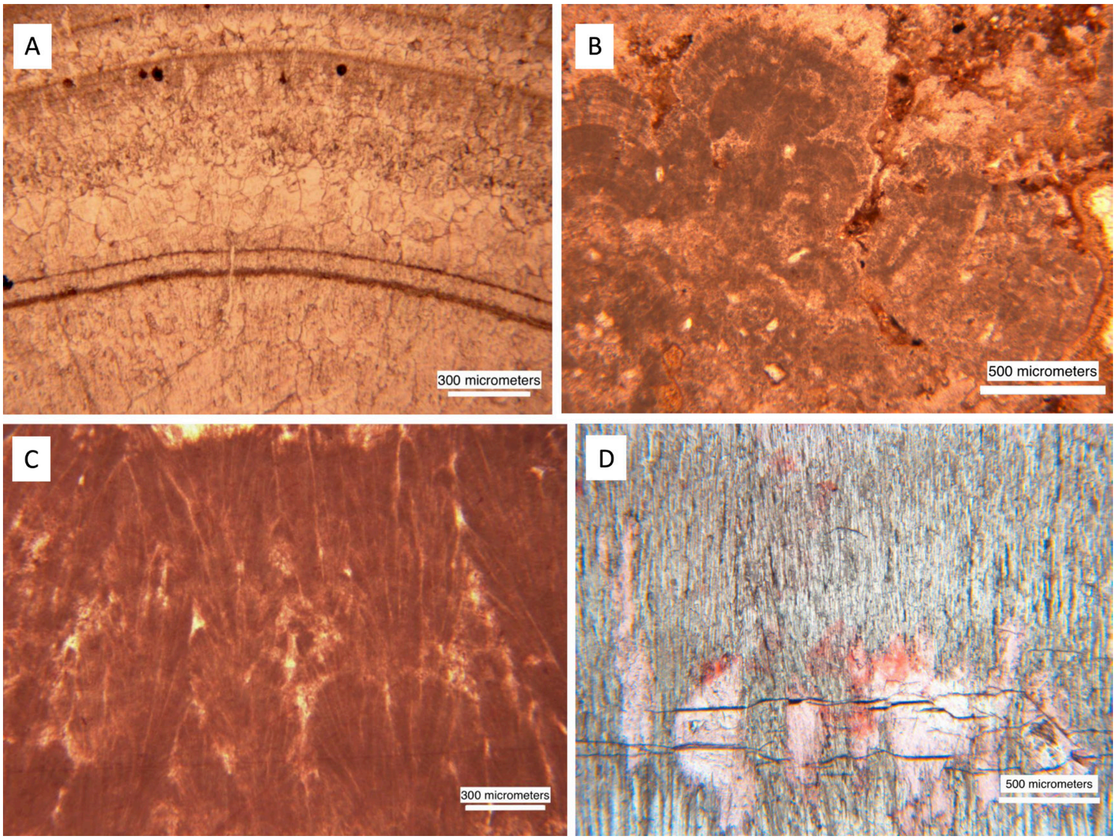

FIG. 14. Stained thin sections from Chintoraste. **A.** Predominantly equant calcite crystals with thin mud and/or microbial interlaminations. **B.** Microstromatolites composed of dark microbial shrub forms in calcite matrix with sparse angular quartz silt grains. **C.** Botryoidal mosaic of elongate, fan shaped calcite crystals. **D.** Thin section showing elongate aragonite crystals being replaced by calcite (pink-white patches), particularly adjacent to fractures and veins, as illustrated here.

in $\delta^{18}O$ (Fig. 16A). At Chintoraste, tufa samples with high $\delta^{13}C$ are located in and close to the main central fissure, whereas samples with high $\delta^{18}O$ are located around a knob about 100 m to the south of this fissure. Other Chintoraste samples have slightly lower $\delta^{18}O$, by about 2‰, whereas their $\delta^{13}C$ is lower by nearly 4‰ (Fig. 16A). These variations suggest that distance from the central fissure influenced isotopic values recorded in the carbonate (cf. Fig. 11A). The $^{87}Sr/^{86}Sr$ values of the carbonate at both spring locations show a narrow distribution, and they are distinct from each other. At El Sifón, $^{87}Sr/^{86}Sr$ is 0.707682±0.000344 (2σ, n=5), while at Chintoraste is 0.706679±0.000307 (2σ, n=6) (Table 2).

5. Discussion

5.1. El Sifón

The thick succession of relatively homogeneous aragonite layers at the El Sifón site indicates rapid carbonate precipitation. Tufa precipitation rates can be as high as 14 mm yr^{-1} in an example from Spain, although 7-8 mm yr^{-1} may be more common (Arenas *et al.*, 2018). Detrital lenses in the El Sifón tufa suggest that carbonate precipitation was interrupted by transient events, such as floods, capable of eroding and transporting sand, silt and mud to the spring site. Broken fragments of laminated aragonite indicate

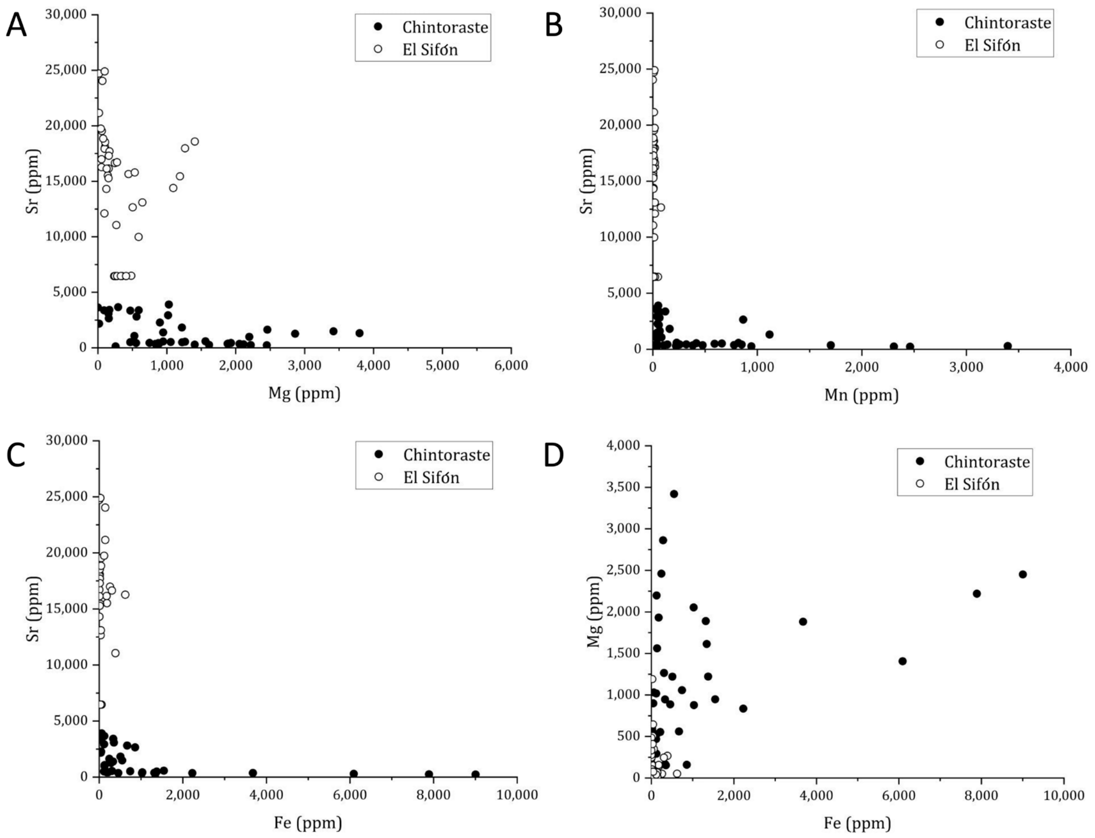

FIG. 15. Cross plots of ICP-OES geochemical results from each tufa location, values are in ppm. **A.** Sr versus Mg. Chintoraste tufa samples are characteristically depleted in Sr relative to El Sifón and have a wider range of Mg values. **B.** Sr versus Mn. El Sifón samples have tightly constrained, low concentrations of Mn, whereas Chintoraste samples are typically lower in Sr, and cluster between 30 and 500 ppm Mn, but also exhibit higher concentrations of Mn, exceeding 2,000 ppm in three samples. **C**-**D.** Sr versus Fe and Mg versus Fe, with El Sifón enriched in Sr relative to Chintoraste and relatively low (<1,000 ppm) Fe concentrations, whereas Chintoraste samples exhibit a wider range of Fe and Mg values.

that these events were severe enough to break up strata, creating breccias and intraclast-rich deposits. Alternatively, or likely in addition, syn-depositional fault-generated movement was sufficient to break up travertine, producing fault breccias, including large (meter-scale) slabs of fractured tufa along the fault slope. Botryoids inside of cavities imply a process whereby strata were formed discontinuously, leaving void spaces. The cavities have smooth interiors, lacking pits or jagged crystal terminations, indicating that they were not formed by significant erosion or chemical dissolution. Cavities more typically occur parallel to bedding, in distinct horizons, with relatively flat floors. They formed as syndepositional openings, akin to submarine neptunian voids that represent tectonic activity or shelf margin instability (Winterer and Sarti, 1994). In this case, fault movement likely generated substrate instability, producing both cavities and breccias. According to Aissaoui (1985), similar large, aragonite botryoidal mamelons from Pleistocene marine reefs formed within fracture cavities, dissolution voids, and intercoralline spaces, but he also described botryoids that formed in karst limestone from freshwater.

The El Sifón tufa facies vertical and lateral variations may represent distance from the active spring water source. A decrease in water temperature and rate of carbonate precipitation occurs as distance from a fault-hosted water source increases (Atabey, 2002; Capezzuoli *et al.*, 2014). The El Sifón example

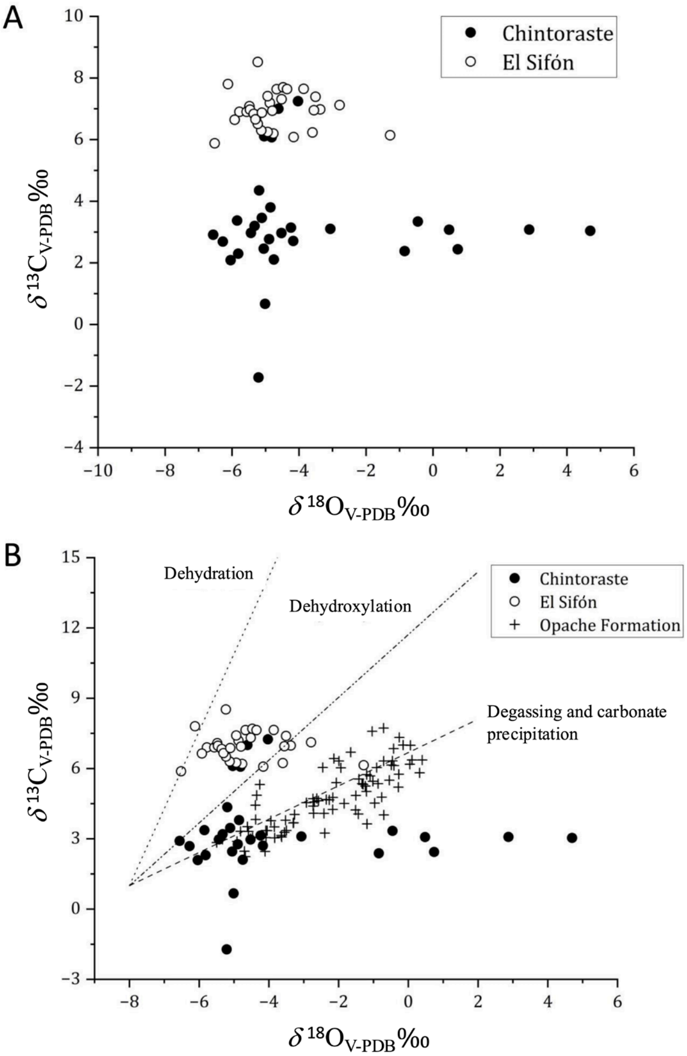

FIG. 16. **A.** Stable isotope cross plot comparing samples from El Sifón and Chintoraste spring deposits. El Sifón values are tightly constrained while Chintoraste values are more variable. **B.** Stable isotope cross plot comparing El Sifón and Chintoraste spring deposits to the approximately contemporaneous palustrine to lacustrine Opache Formation limestones. Included are the increasing isotope evolutionary trends of remaining dissolved inorganic carbon for processes discussed in the text: dehydration, dehydroxylation, and degassing, with carbonate precipitation. Data for the Opache Formation from de Wet *et al.* (2015, 2019).

of a 30 cm thick layered succession transitioning from acicular aragonite to detrital sands and muds, with microstromatolite and micritic-rich intervening horizons, is interpreted as lateral migration of the water source farther from the sample location over time. As fractures closed due to infilling by carbonate precipitation, new fractures opened, shifting the water source and bringing groundwater to the surface nearby.

Microstromatolitic laminations represent cyanobacterial colonization with bio-induced or bio-mediated $CaCO_3$ precipitation. Light and dark alternations of micritic fabrics are interpreted as representing seasonal changes with lighter, more porous laminations forming in cooler months, and darker, dense sparry laminations forming more rapidly in warmer months (Jones and Renaut, 2010), although Matsuoka *et al.* (2001) found the reverse pattern in a Japanese tufa. Cyanobacterial/bacterial growth produces dark, organic-rich laminations, with intervening thin bands of abiotic micrite or spar, and these alternations are particularly apparent in climates with strong seasonality (Kano *et al.*, 2004; Jones and Renaut, 2008; Wang *et al.*, 2022). Such laminations may also be due to cyclic changes in source water flow and velocity, which may or may not be related to seasonal changes (Jones and Renaut, 2008; Wang *et al.*, 2022). Previous research on Opache Formation lacustrine and palustrine stromatolites with similar alternations are interpreted as indicating seasonal changes which influenced source water flow and $CaCO_3$ precipitation rate (de Wet *et al.*, 2015).

There is little evidence for an extensive biota living within the El Sifón tufa. The diatom assemblage is sparse and indicative of water conditions generally unfavorable to a diverse diatom community, and microbial deposits are limited to microstromatolitic laminations within some aragonite crystal layers. Very rapid aragonite precipitation rates, coupled with very high solute concentrations may have inhibited diatom and microbial colonization. In general, the scarcity or complete absence of diatom valves in spring samples indicates unfavorable conditions for either diatom growth or diatom preservation. At El Sifón, the diatoms in samples with scarce abundance are all benthic, indicating shallow water. The dominant species were *Nitzschia inconspicua*, *Planothidium delicatulum*, and *Staurosirella pinnata*. *Nitzschia inconspicua* is a euryhaline species, with a wide tolerance to salinity. It has been found in oligosaline (1.4 to 5.3 mS/cm) ponds (Fernández-Moreno *et al.*, 2022) and habitats with high alkalinity (~200 mg/L $CaCO_3$) and conductivity (988 µS/cm) (Trobajo *et al.*, 2013). *Planothidium delicatulum* is also associated with higher salinities (Fernández-Moreno *et al.*, 2022) and waters with low organic content (Sawai *et al.*, 2017). *Staurosirella pinnata*, a small colonial fragilariaceae (*sensu lato*), has a broad salinity tolerance (Marohasy and Abbot, 2015) and might prefer springs with sandy substrates and lower dissolved oxygen (Wojtal and Sobcyk, 2012). Diatom growth is hindered at water temperatures above 60 °C (Brown and Fritz, 2019). Warm spring fluid interaction with sediment could result in dissolution of biogenic silica (Brown *et al.*, 2019), as could high salinity and carbonate precipitation (Ryves *et al.*, 2006). Therefore, it is possible that diatoms were living in the spring waters but were dissolved after death, or that conditions were not favorable for diverse diatom communities due to warm temperature, high salinity, and/or high alkalinity. At El Sifón, high concentrations of trace elements in the associated aragonite suggests that high conductivity may also have hindered diatom growth.

Mudcracks on the upper Opache surface indicate that tufa deposition ceased. Water flow was either diverted elsewhere when the fault and fracture system became occluded with carbonate, the climate shifted towards greater aridity, or a change in regional hydrology led to negligible water flow to the site. Elsewhere in the Calama Basin, the Opache Formation's uppermost surface is also mudcracked, suggesting that the main factor in ending Opache Formation carbonate deposition was a regional shift towards drier conditions (de Wet *et al.*, 2019).

Groundwater aquifers in the Calama and Turi basins are fed by precipitation in the Western Andes catchment area (Jordan *et al.*, 2015; Houston, 2023). At the time of Opache Formation deposition groundwater circulating through the Andean arc was associated with heightened volcanic activity. The *in situ* ignimbrite weathering surface at the contact between the underlying Sifón Ignimbrite and the tufa (Fig. 5) shows alteration and dissolution by surface and/or groundwater after the ignimbrite was emplaced. Houston (2023) reported that groundwater traveled along the Sifón Ignimbrite-Opache Formation contact, with the ignimbrite serving as an aquiclude. Subsurface water moving along the contact may have come to the land surface where it intersected with the Divisoco Fault System, forming the El Sifón spring. This is consistent with the field evidence showing the close association of the ignimbrite surface, faults and local fractures, and carbonate distribution. As reported elsewhere, faults may serve as conduits for groundwater to debouch at the land surface, driving carbonate precipitation by degassing (Baker and Smart, 1995; Camuera *et al.*, 2015; Lopez *et al.*, 2017; Quade *et al.*, 2017). At El Sifón, the Divisoco Fault System's surface expression is a distinct break in slope; bedding in the tufa dips down the fault slope and slabs of tufa are fragmented down slope, further supporting the close connection between the spring carbonate and active fault tectonics. Therefore, evidence indicates that the fault system at El Sifón served as a conduit for groundwater to rise to the surface, debouching at the break in slope, degassing and driving tufa precipitation.

The presence of non-ferroan carbonate in El Sifón thin sections, based on staining, confirms the ICP-OES results showing that the El Sifón limestones have low iron concentrations (Fig. 15; Table 1). ICP-OES results show low Mn values as well (Fig. 15; Table 1). These low values indicate that the tufa formed under oxidizing conditions whereby Mn was scavenged into abundant MnO deposits, and iron, if present in the porefluids, was similarly in an oxidized state, and therefore, inaccessible for inclusion the carbonate. In contrast, Mg, and particularly Sr, concentrations from the El Sifón tufa are high (Fig. 15; Table 1). Groundwater interaction with Neogene and younger volcanic activity throughout the arc, and particularly with the Sifón Ignimbrite, could have provided Mg and Sr for the spring waters; however, none of these rocks have exceptional Mg or Sr concentrations (Álvarez *et al.*, 2023), which suggests there must be an additional source for these cations (as discussed in *Geochemistry* below).

5.2. Chintoraste

Although the depositional setting at Chintoraste is broadly similar to that at El Sifón, with faults and fractures bringing CO_2-rich subsurface water up to the land surface, the facies at Chintoraste are more diverse. The tufa's association with two fissure ridges indicates that fissure springs constructed tufas with relief above the surrounding area, and the presence of microterracettes, ripple marks, and flowstone show that water flowed downhill off the ridges. Within and directly adjacent to the mound fissures, laminated calcite with aragonite botryoids indicates rapid, inorganically mediated carbonate precipitation, but more distal to the veins, the presence of oncolites and stromatolites indicates that waters were conducive to microbial colonization (Martin-Bello *et al.*, 2019). Probable plant remains, tentatively identified as a water lily-type plant (C. Williams, personal communication, 2020), suggest that locally there were ponds or slow-moving water. Sands and silty mudstones indicate intermittent periods of surface water flooding capable of transporting detrital material onto the lower elevation portions of the tufa complex. Similar to those observed at El Sifón, mudcracks on the upper Opache Formation surface at Chintoraste indicate that tufa deposition ceased, reflecting a shift towards drier conditions.

Porewaters within the Chintoraste tufa episodically became reducing based on the presence of ferroan calcite zones within calcite crystals, with relatively enriched Mn^{2+} and Fe^{2+} values relative to those from El Sifón (Fig. 15; Table 1). Some Mn was incorporated into MnO dendrites which are common in the tufa, but reduced valence Mn^{2+} was also available as a trace element within the tufa calcite. Trace element sources at Chintoraste include Jurassic marine limestone in the catchment area (Duhart *et al.*, 2018), as well as Eocene volcanic rocks, which may have provided Fe and Mn ions to the spring water. Marine limestone is typically low in Mn and Fe (Veizer, 1983), but groundwater usually contains between 0.1 and 100 ppm Mn (Veizer, 1983). Mn^{2+} and Fe^{2+} concentrations measured from the Chintoraste tufa are higher than expected for typical freshwater carbonates which indicates that an additional Mn and Fe source must have contributed ions to the Chintoraste spring water. The underlying Icanche Formation consists of volcanic deposits (Jordan *et al.*, 2015; Duhart *et al.*, 2018), thus groundwater moving in fractures through the volcanics is a likely source, similar to Gibert *et al.*'s (2009) interpretation that volcanic deposits provided ions for Quaternary carbonate spring deposits in Argentina.

Dissolution of marine carbonates may contribute ions to groundwater, yielding relatively high Sr^{2+} and Mg^{2+} values in freshwater limestones (Camuera *et al.*, 2015), and likely was a significant source for Mg and Sr in Chintoraste spring water (as discussed further in *Geochemistry* below). Jordan *et al.* (2015) and Houston (2023) documented an upper and lower aquifer within the Calama Basin, fed by rainfall in the Precordillera. Faults accessed these aquifers (Jordan *et al.*, 2015), and the Chintoraste tufa's location on the eponymous fault indicates that groundwater, enriched in trace elements, was the primary fluid for tufa formation. As groundwater debouched at the surface, CO_2 degassing would have been the first mechanism to drive carbonate precipitation, as seen in the field evidence for laminated calcite and aragonite proximal to the veins. Physicochemical and bio-mediated calcite precipitation occurred more distal to the veins, producing the oncolite and stromatolite facies. Surface water, associated with flood events, transported detrital grains and created brecciated horizons, but also provided additional water that contributed to tufa growth.

Similar to El Sifón's aragonite botryoids, botryoids at Chintoraste also line the inside of non-erosional cavities, suggesting fault-generated movement created void spaces that were rapidly infilled with the precipitation of aragonite crystals. Horizons of curved and contorted laminae are concentrated close to fractures, suggesting small-scale tectonic movement created void spaces that were rapidly cemented with aragonite and/or calcite, coeval with substrate mobility. Parrish *et al.* (2019) noted that carbonate fans of radiating crystals indicate rapid precipitation rates in spring systems.

In general, the scarcity or complete absence of diatom valves in spring samples indicates unfavorable conditions for either diatom growth, or diatom preservation. As at El Sifón, the Chintoraste diatoms with scarce abundance are benthic, indicating shallow water. Tufas from Chintoraste have relatively less biogenic silica (diatom valves, chrysophyte cysts, sponge spicules, phytoliths) than El Sifón, suggesting the El Sifón paleoenvironment may have been more conducive to preserving silica. Warm spring fluid interaction with sediment could also result in diagenetic alteration of biogenic silica (Brown *et al.,* 2019). High salinity and carbonate precipitation are also common causes for diatom dissolution (Ryves *et al.,* 2006).

5.3. Stable isotopes

Dissolved inorganic carbon (DIC) in the predominantly pH neutral to moderately alkaline waters of northern Chile is HCO_3^- (Stumm and Morgan, 1995). The isotopes of C and O fractionate due to both the crystallization of $CaCO_3$ and the liberation of CO_2:

$$2HCO_3^- + Ca^{2+} \leftrightarrow CaCO_3 + CO_2 + H_2O \qquad (1)$$

If the precipitation of $CaCO_3$ is inhibited, or the rate of formation is slower than the rate at which CO_2 degasses, then isotopes are affected by the dehydration of HCO_3^- at pH below 8.6:

$$HCO_3^- + H^+ \leftrightarrow H_2CO_3 \leftrightarrow H_2O + CO_2 \qquad (2)$$

Or dehydroxylation at pH above 8.6:

$$HCO_3^- \rightarrow CO_2 + OH^- \qquad (3)$$

However, the rate of exchange of O isotopes between CO_2 and H_2O often takes longer than the flux of bicarbonate to the surface, so the effects of degassing on O isotopes are smaller than expected, especially compared to C isotopes (Carlson *et al.*, 2020). Furthermore, as precipitation of $CaCO_3$ is more likely to follow equilibrium conditions because degassing is kinetic, C isotopes more commonly exhibit degassing (Carlson *et al.*, 2020). In terrestrial systems, the role of pCO_2 is particularly important in defining $\delta^{13}C$ because it is highly variable, and it affects degassing rates (Marx *et al.*, 2017). Equilibrium fractionation factors are well known for the reactions that affect the isotope composition of carbonate spring deposits (Romanek *et al.*, 1992; Kim and O'Neil, 1997; Zhou and Zheng, 2003). Kinetically driven isotope effects are less well known but tend to be 2-3 times greater than equilibrium (Kele *et al.*, 2015; Guo and Zhou, 2019). The C and O isotope evolution of HCO_3^- during precipitation of $CaCO_3$ can be predicted for different temperatures, and assuming precipitation of $CaCO_3$ occurs at isotopic equilibrium, can be compared with our data.

Chintoraste isotopic data indicate that calcite precipitation and degassing occurred at similar rates, in contrast to results from El Sifón (Fig. 16B). Some of the samples furthest from the fissures at Chintoraste indicate that evaporation, which increases $\delta^{18}O$, also occurred. Samples with elevated $\delta^{13}C$, indicative of degassing, dominate the isotope composition of El Sifón, with only samples distal from the main spring site suggesting carbonate precipitation occurred at similar rates to degassing. The El Sifón samples lie between the dehydration and dehydroxlation trends, which could be accounted for by the consumption of acidity in reaction (2) and the switch to reaction (3). Cross-bedded sandstone interbedded with tufa at the El Sifón location indicates that surface water flow provided freshwater to the tufa-precipitating spring, but the observed $\delta^{13}C$ values require that most of the spring water must have been sourced from sufficient depths such that it did not acquire significant quantities of soil-derived CO_2 (Godfrey *et al.*, 2021).

Assuming the samples with the lowest $\delta^{13}C$ and $\delta^{18}O$ are most representative of samples that precipitated with the least amount of degassing, then the source of HCO_3^- appears to be similar at both locations. In addition, assuming equilibrium conditions for $CaCO_3$ precipitation, the $\delta^{13}C$ and $\delta^{18}O$ at the sites are very similar to the composition of modern springs within the Central Andean arc (Godfrey *et al.*, 2021; Herrera *et al.*, 2021). However, given the volume of carbonate precipitated at El Sifón and Chintoraste compared to the modest amount of modern barrage river tufa, the chemical composition and/or fluxes of the water discharged at each location were clearly different than today.

5.4. Fault-related springs and groundwater movement

Springs are an important component in the Atacama Desert region's natural water distribution system, bringing groundwater from the Andes into the desert where it may be released from aquifers at spring sites (Houston, 2007, 2023). The role of tectonism in determining the location of springs is documented from several tectonically active basins elsewhere, such as the Teruel Basin in Spain (Camuera *et al.*, 2015), the Barrancas Blancas in Chile (Quade *et al.*, 2017), and Obruktepe (Denizli Basin) in Turkey (Lopez *et al.*, 2017). Circulating groundwaters can become enriched in carbonate ions through dissolution of pre-existing limestone or introduction of geogenic/magmatic deposits, driven by CO_2 gas under high hydrostatic pressure, which facilitates dissolution (Cappezuoli *et al.*, 2014). Precipitation of calcium carbonate occurs when groundwater rich in CO_2 is discharged at the surface.

This study provides additional information about potential water sources for the Calama Basin's extensive Opache Formation carbonate depositional system. The Chintoraste spring was likely a significant water source for the formation's western palustrine depositional environment. The spring at El Sifón moved surface and groundwater from the Turi Basin into the ancestral Salado River or its predecessor (Fig. 17). Impermeable, locally welded Miocene ignimbrites (*e.g.*, Sifón) are overlain by porous and permeable sedimentary successions (*e.g.*, Opache, Toconce) that host unconfined phreatic aquifers which form a regional near-surface system (Houston, 2007). This supports local field evidence that at El Sifón, groundwater moved above the Sifón Ignimbrite, within Opache Formation sediments and weathered

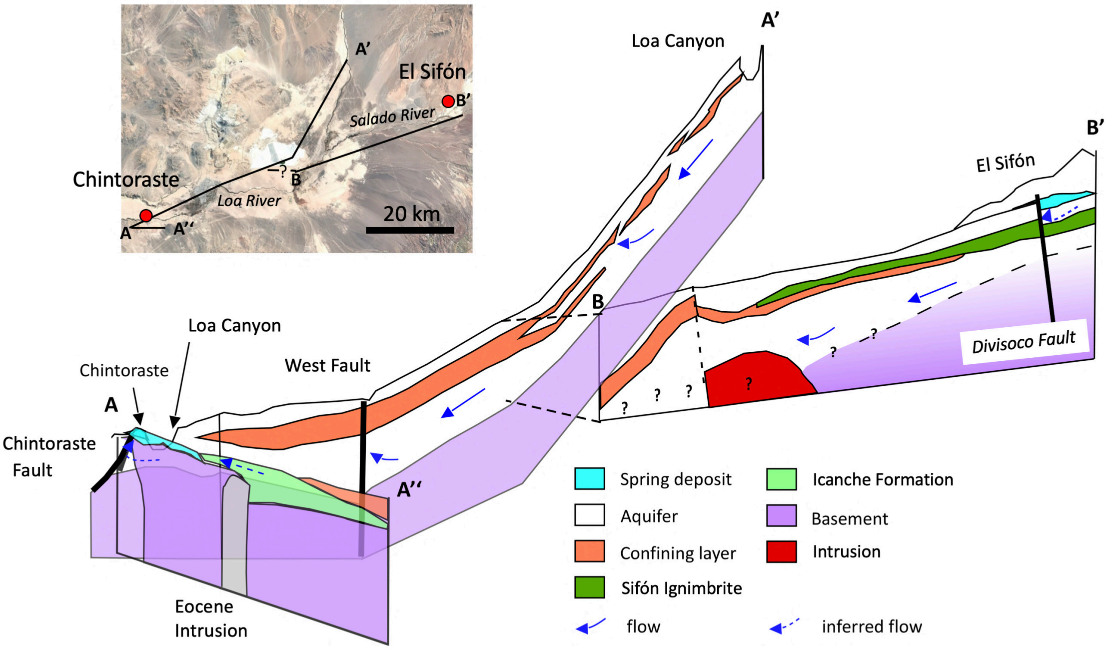

FIG. 17. Schematic geohydrology cross sections across the Calama and Turi basins, based on Houston (2007), Jordan *et al.* (2015), Bulboa (2017), and Duhart *et al.* (2018). A-A' and A-A'' sections terminate close to the Chintoraste paleospring system, showing potential flow paths across the Calama Basin (A-A') and across the Chintoraste hill (A-A''). The Loa canyon had not yet developed at the time of spring activity. B-B' is the cross section that links the El Sifón paleospring system at the western edge of the Turi Basin and the Calama Basin. Question marks highlight the areas where there is considerable uncertainty as to the structural geology, and hence groundwater flow paths.

ignimbrite, to be released at the El Sifón spring site (Fig. 17). Both El Sifón and Chintoraste fossil springs provide additional evidence that the Late Miocene-Pliocene was a period of wetter conditions in the region, with wet-dry alternations in an arid to semi-arid regime, rather than today's hyperarid conditions (see discussions in Sáez *et al.*, 2012; de Wet *et al.*, 2015, 2019; Evenstar *et al.*, 2015).

5.6. Geochemistry

Limestone precipitated at El Sifón and Chintoraste consist of different polymorphs of calcite; predominantly aragonite at El Sifón, and predominantly calcite at Chintoraste (aragonite and calcite were identified petrographically and confirmed by XRD analysis of several samples; Table 1). Aragonite is often ascribed to hydrothermal carbonate precipitation, as an indication of warm spring water (Kitano, 1962; Folk, 1994; Minissale *et al.*, 2002), but the oxygen isotopic signature of the El Sifón tufa aragonite does not suggest that the spring waters were warmer than ambient temperature. The tufa deposits at Chintoraste are largely calcite, yet have a generally similar $\delta^{18}O$ signature to the El Sifón tufa. This study's aragonite vs calcite paradox cannot, therefore, be explained by spring water temperature alone. As discussed in Jones and Renault (2010), Della Porta (2015), and Alonso-Zarza *et al.* (2021), other factors such as precipitation rate, pCO_2, water agitation, Mg/Ca ratios, and microbial interactions may all affect which polymorph precipitates. Since El Sifón and Chintoraste are coeval (at least within the same formation), external factors such as climate would have been essentially the same at each site. Guo and Riding (1992) suggested that aragonite laminae in Rapolano Terme travertines (Italy) precipitated from ambient temperature waters driven by microbial activity. At El Sifón, however, evidence for microbial activity is scant compared to that from Chintoraste, so it is unlikely that microbial activity drove aragonite precipitation there. Our ICP-OES results show an enrichment in Mg relative to typical groundwater (Veizer, 1983) so a high Mg/Ca ratio might have contributed to aragonite precipitation at El Sifón. In addition, field evidence shows that the Divisoco Fault System was active coeval with El Sifón spring deposition. In fact, breccias and slabs of fractured and re-cemented tufa are present on the downthrown side of the fault, suggesting that episodic tectonics may have created water turbulence, so water agitation may also have been a contributing factor in favoring aragonite precipitation over calcite at El Sifón. Spring discharge of CO_2-rich groundwater, leading to $CaCO_3$ precipitation, produced carbonate tufa at both locations, and episodic high discharge rates may also have been a factor in whether the aragonite or calcite polymorph formed. Rapid aragonite precipitation rates for the El Sifón spring are indicated by the likely short time frame for its deposition, based on U-Pb dates obtained from the base and near the top of the tufa (Fig. 18; Table 3). Chen *et al.* (2004) suggest that high discharge rates and water turbulence are significant factors in the formation of tufa in modern springs. Further study is needed to fully understand the factor(s) contributing to aragonite vs. calcite precipitation at the El Sifón and Chintoraste springs.

Post-depositional diagenesis had a greater effect at Chintoraste than at El Sifón. Petrography of Chintoraste stained thin sections shows botryoid crystals partially converted to calcite, indicating diagenetic conversion of aragonite (Fig. 14D), similar to calcite pseudomorphs after aragonite described from spring carbonate in the Argentinean Andes (Gibert *et al.*, 2009). Aragonite conversion to calcite was not observed in El Sifón thin sections. By comparison, an absence of aragonite at Barrancas Blancas tufa, ~270 km south of Chintoraste (Quade *et al.*, 2017), suggests that there all of the aragonite converted to calcite diagenetically, if it was ever present. The multi-million-year duration of precipitation at Barrancas Blancas (Quade *et al.*, 2017) implies a long-lived groundwater supply that may not have been conducive to aragonite precipitation, or, if aragonite had been present, allowed for ample time for diagenesis to have converted the aragonite to calcite (Gibert *et al.*, 2009).

The crystal structure of aragonite characteristically allows for Sr cation substitution for Ca more readily than calcite (Viezer, 1983). All of our tufa samples, whether from Chintoraste or El Sifón, contain relatively high concentrations of Sr (average 1,424 ppm, maximum 3,656 ppm; average 14,871 ppm, maximum 24,901 ppm, respectively) (Table 1), in comparison with marine aragonite, which typically ranges from ~7,000 to 10,000 ppm Sr (Veizer, 1983; Aissaoui, 1985). Aissaoui's (1985) study of freshwater botryoidal aragonite in karst near the Egyptian margin of the Red Sea (Um Gheig locality) may

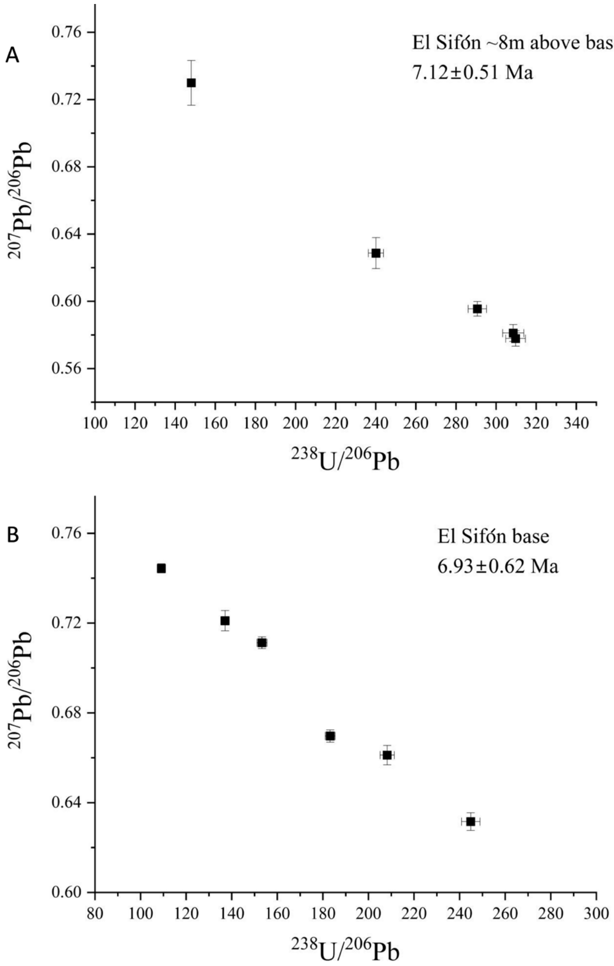

FIG. 18. Tera-Wasserburg plots of U-Pb isotopes from two samples of El Sifón tufa. **A.** 8 m above the uppermost level of the tufa deposit. **B.** At the lowest exposed level of the outcrop. Error bars indicate age uncertainties at the 2σ level range

offer some insight as he noted that the botryoids there contained particularly high concentrations of strontium (average 13,600 ppm). Aissaoui (1985) suggested that the high Sr originated from celestite associated with locally occurring lead-zinc ores. Although the botryoids described by Aissaoui (1985) are similar to those from El Sifón in size and shape, and in having elevated Sr concentrations, celestite has not been found at El Sifón, so another Sr source must have been present, as discussed below.

Elevated strontium concentrations in spring water and spring deposits have been used to identify limestone, and in some instances, anhydrite, that groundwater interacted with prior to forming travertine in Italy (Minissale, 2004). Sr in the water where travertine actively forms in Italy is higher than has been measured in groundwater in the Calama Basin (Godfrey *et al.*, 2019), but Calama Basin groundwater Sr levels could have been higher in the past, as suggested by δ^{11}B results (Godfrey *et al.*, 2019). In the Antofagasta Region near the city of Calama, most of the modern near-surface aquifers are in volcanic rock (Godfrey *et al.*, 2019). Based on high δ^{11}B sampled from local water, Godfrey *et al.* (2019) proposed that Late Cretaceous marine limestones, such as those of the Yacoraite Formation (Marquillas *et al.*, 2007), may underlie much of the late Cenozoic volcanic arc, and could react with deeply circulating groundwater to impart the high δ^{11}B typical of marine carbonate (Barth, 1993) to groundwater. At the time when the El Sifón carbonate spring was active, most of the volcanoes that now define the northern edge of the Turi Basin were not present, so groundwater may have accessed the Cretaceous limestone more readily. The similarity of the Sr isotope composition of ignimbrites (*e.g.*, Kay *et al.*, 2010) and Cretaceous seawater (Veizer, 1989) leaves some ambiguity as to the El Sifón Sr source, but the elevated Sr concentrations in tufa there imply involvement of a source that was more enriched in Sr than the rocks that currently weather and supply solutes in the area, since such high Sr concentrations are not found in groundwater there now (Romero *et al.*, 2003; Godfrey *et al.*, 2019). Thus, the shallow marine Late Cretaceous limestone of the Yacoraite Formation, which crops out extensively in Argentina (Marquillas *et al.*, 2007) and may underlie the Turi Basin region, is the most probable source for elevated Sr values from El Sifón aragonite. The Sr content of the Yacoraite Formation limestone varies between 328 and 24,000 ppm (Marquillas *et al.*, 2007), and while evaporites have not been reported for sections in Argentina, diagenetic Sr-rich barite macrocrystals have been reported, suggesting replacement of primary sulfates (Marquillas *et al.*, 2007). Assuming the Yacoraite Basin shallowed to the west, away from the open ocean connection, it is possible that the extent of sediments rich in Sr also increases westward and potentially underlie the modern arc in Chile (Matthews *et al.*, 1996), suggesting that Sr-rich groundwater may have reached the Turi Basin.

A previous study of Antofagasta regional spring waters found high DIC and enriched $\delta^{13}C$, but did not distinguish between geogenic CO_2 in terms of mantle or devolatilized limestone (Godfrey *et al.*, 2021). At the Paniri spring (~20 km NE of El Sifón), elevated $\delta^{11}B$ suggested a marine source of B (Godfrey *et al.*, 2019). Minissale (2004) interpreted similar high Sr values in the Italian travertine as an indication that deep fluid circulation dissolved Tethyan limestone and anhydrite, producing Sr-rich groundwater that debouched at spring sites. Similarly, the extremely high Sr concentrations within aragonite from El Sifón can only be reconciled with the involvement of dissolved marine carbonate, and B, $\delta^{11}B$, and Sr isotope data from the Antofagasta region (including the Turi Basin) indicates that groundwater interacted with marine limestone (±evaporite deposits), producing Sr-enriched spring water.

Chintoraste aragonite samples have elevated Sr concentrations (although not as high as those from El Sifón aragonite tufa) but are similar to Italian spring carbonate where Sr values are interpreted to be derived from older marine limestone (Minissale, 2004). A similar mechanism is plausible for the Chintoraste tufa because of its proximity to marine Jurassic limestone (Duhart *et al.*, 2018). The Chintoraste Fault (Duhart *et al.*, 2018) influenced the Chintoraste spring system as the tufa deposits are tilted and fractured, and carbonate-filled veins cut through the tufa, indicating that groundwater containing $CaCO_3$ moved through the fault fracture system from some depth. The Sr isotope composition measured from Chintoraste tufa is also consistent with Jurassic limestone occurring around the Chintoraste site (*e.g.*, Moctezuma and Cerro Campamento formations; Duhart *et al.*, 2018), suggesting that marine carbonate contributed Sr to groundwater that reached the surface as the Chintoraste spring.

5.4. Aquifers

The similar oxygen isotope composition of the two spring sites, despite their geographic separation, suggests that they may have been connected through a subsurface path or shared a common genetic mechanism (Fig. 17). Water flow in the phreatic aquifer as it descends to the Calama Basin is split by confining layer, resulting in two aquifers, denominated as Upper and Lower aquifers (Jordan *et al.*, 2015; de Wet *et al.*, 2022; Houston, 2023) (Fig. 17). East of the West Fault, the hydraulic head is considerably higher in the Lower Aquifer than the Upper Aquifer, indicating there is a competent confining layer, but at the West Fault the hydraulic heads equilibrate, indicating water exchange between the two aquifers. To the east, the Upper Aquifer is hosted by the Opache Formation limestone as well as the Chiquinaputo Formation. The Opache Formation, dated by ashes between 5.76±0.10 and 3.37±0.06 Ma (May *et al.*, 1999, 2005), is limited to the flat-lying areas and extends east into the Turi Basin area, where it intercalates with conglomerates of the uppermost member of the Chiquinaputo Formation (Tomlinson *et al.*, 2018; Álvarez *et al.*, 2023). East of this area, ignimbrites and clays separate a phreatic and confined aquifer, but a break in the confining unit allows some water to ascend across it (Bulboa, 2017).

The El Sifón spring site mostly overlies the ~9-7.5 Ma Sifón Ignimbrite but its westernmost part also overlies sediments of the Chiquinaputo Formation (Álvarez *et al.*, 2023). The Chintoraste site lies to the west of the West Fault and is located on what was the very edge of the Upper Aquifer in the Opache Formation. The El Sifón site lies well to the east of the Calama Basin aquifers, and today water in the Turi Basin flows into either the Salado River or contributes to groundwater that reaches the Calama Basin through the Chiquinaputo Formation (Houston, 2023). A subsurface groundwater-derived dissolution channel has been suggested to run south, roughly parallel to the Loa River east of Calama (Bulboa, 2017), although it is unknown if this channel continues west to the Turi Basin (Fig. 17). However, our limited number of Sr isotope results that show the Chintoraste carbonate is less radiogenic (0.7067) than tufa from El Sifón (0.7077) (Table 2), suggesting that even if there is a subsurface connection today, during the Miocene, the spring waters were sourced from different aquifers.

6. Conclusions

Fossil spring sites at Chintoraste and El Sifón were fault-related fissure-type springs where groundwater debouched, degassed, and precipitated calcite and aragonite. At Chintoraste, evidence for flowing surface water such as ripplemarks and microterracettes indicate surface water flow, confirmed by the presence of stromatolites, oncolites, and possible plant fragments indicating oxygenated conditions for microbial and plant communities. Chintoraste spring water contributed to the Opache Formation's palustrine depositional environments.

Field relations at El Sifón indicate that groundwater traveled along the permeable weathered top of the Sifón Ignimbrite until intersecting the Divisoco Fault System, where fluid moved upward to debouch through fractures and fissures. The El Sifón spring may also have contributed water into the Opache depositional environment via groundwater or surface flow between the Turi and Calama basins but this remains to be verified.

$\delta^{18}O$ and $\delta^{13}C$ values, Sr isotopes, and trace elements measured from calcite and/or aragonite from the two tufa locations indicate that there were different water sources for each spring site. Differing spring water chemistry, in conjunction with kinetic factors, such as discharge rate and water turbulence, produced primarily aragonite at El Sifón, and mostly calcite at Chintoraste, although diagenesis resulted in some aragonite to calcite conversion at Chintoraste. Geochemical results from this study suggest that older marine limestones (±evaporites) were dissolved by circulating groundwater to enrich spring water with Sr and Mg, and interaction with volcanic rocks supplied additional Fe and Mn to groundwater feeding the springs during the Miocene.

Both locations have aragonite botryoids, an unusual freshwater carbonate morphology. Rapid rates of precipitation may have been the primary factor for producing this cm-scale, coalesced crystal fan morphology, although Sr concentrations within them are unusually high, suggesting that elevated cation values could have also contributed to their formation.

Acknowledgments

We appreciate funding and support provided by Franklin & Marshall College research grants to Caterham, Lee, Hicks, and Mumby, and funds from the F&M Geoscience Founders Society. Thanks to E. Wilson for assistance using the ICP-OES at Franklin & Marshall College and Richard Mortlock at Rutgers University for isotope assistance. T. Rasbury at SUNY-Stony Brook University kindly provided U-Pb analysis. Thank you also to three reviewers who made valuable suggestions to improve the manuscript and assisted with the Spanish translations.

References

Aissaoui, D.M. 1985. Botryoidal aragonite and its diagenesis. Sedimentology 32: 345-361. doi: https://doi.org/10.1111/j.1365-3091.1985.tb00516.x

Alsonso-Zarza, A.; Casillas, R.; Rodríguez-Berriguette, Á. 2021. Landscape modification due to agricultural irrigation: carbonate tufa formation on Tenerife, Canary Islands, Spain. Anthropocene 34: 1-13. https://doi.org/10.1016/j.ancene.2021.100285

Álvarez, P.; Tunik, M.; Giambiagi, L.; Rodriguez, C. 2023. Geología de las áreas Cupo-Toconce y Cerros de Tocopuri. Servicio Nacional de Geología y Minería, Carta Geológica de Chile, Serie Geología Básica 215-216: 223 p. 1 mapa escala 1:100,000. Santiago.

Arenas, C.; Osácar, M.C.; Augué, L.F.; Andrews, J.E.; Pardo, G.; Marca, A.; Martín-Bello, L.; Pérez-Rivarés. 2018. Seasonal temperatures from $\delta^{18}O$ in recent Spanish tufa stromatolites: Equilibrium redux! Sedimentology 65: 1611-1630. https://doi.org/10.1111/sed.12440

Ashley, G.M.; de Wet, C.B.; Manuel, D.R.; Karis, A.M.; O'Reilly, T.M.; Baluyot, R. 2014. Freshwater

Limestone in an Arid Rift Basin; a Goldilocks Effect. Journal of Sedimentary Research 84 (11): 988-1004. https://doi.org/10.2110/jsr.2014.80

Atabey, E. 2002. The formation of Fissure Ridge type laminated travertine-tufa deposits microscopical characteristics and diagenesis, kirşehir central Anatolia. Bulletin of the Mineral Research and Exploration 123-124: 59-60.

Baker, A.; Smart, P.L. 1995. Recent flowstone growth rates: Field measurements in comparison to theoretical predictions. Chemical Geology 122 (1-4): 121-128. https://doi.org/10.1016/0009-2541(95)00017-G

Barth, S. 1993. Boron isotope variations in nature: a synthesis. Geologische Rundschau 82: 640-651.

Bertin, D.; Amigo, A.M. 2019. Geología del volcán San Pedro, región de Antofagasta. Servicio Nacional de Geología y Minería, Carta Geológica de Chile, Serie Geología Básica 201: 71 p. 1 mapa escala 1:50.000. Santiago.

Blanco, P.; Tomlinson, A.J. 2009. Carta Chiu Chiu, región de Antofagasta. Servicio Nacional de Geología y Minería, Carta Geológica de Chile, Serie Geología Básica 117: 54 p. 1 mapa escala 1:50.000. Santiago.

Brown, S.R.; Fritz, S.C. 2019. Eukaryotic organisms of continental hydrothermal systems. Extremophiles 23: 367-376. https://doi.org/10.1007/s00792-019-01101-y

Brown, S.R.; Fritz, S.C.; Morgan, L.A.; Shanks III, W.C. 2019. Fossilized diatoms of siliceous hydrothermal deposits in Yellowstone National Park, USA. Diatom Research. https://doi.org/10.1080/0269249X.2019.1698466

Bulboa, I.C. 2017. Analisis Y Conceptualizacion del Acuifero de la Cuenca de Calama Y subcuenca Llalqui, II Region de Antofagasta, Chile. thesis. Universidad de Chile: 135 p.

Camuera, J.; Alsonso-Zarza, A.M.; Rodríguez-Berriguete, A.; Meléndez, A. 2015. Variations of fluvial tufa sub-environments in a tectonically active basin, Pleistocene Teruel Basin, NE Spain. Sedimentary Geology 330: 47-58. https://doi.org/10.1016/j.sedgeo.2015.09.015

Capezzuoli, E.; Gandin, A.; Pedley, M. 2014. Decoding tufa and travertine (freshwater carbonates) in the sedimentary record: The state of the art. Sedimentology 61 (1): 1-21. https://doi.org/10.1111/sed.12075

Carlson, P.E.; Noronha, A.L.; Banner, J.L.; Jenson, J.W.; Moore, M.W.; Partin, J.W.; Deininger, M.; Breecker, D.O.; Bautista, K.K. 2020. Constraining speleothem oxygen isotope disequilibrium driven by rapid CO_2 degassing and calcite precipitation: Insights from monitoring and modeling. Geochimica et Cosmochimica Acta 284: 222-238. https://doi.org/10.1016/j.gca.2020.06.012

Chen, J.; Zhang, D.D.; Wang, S.; Xiao, T.; Huang, R. 2004. Factors controlling tufa deposition in natural waters at waterfall sites. Sedimentary Geology 166 (3-4): 353-366. https://doi.org/10.1016/j.sedgeo.2004.02.003

de Wet, C.; Godfrey, L.; de Wet, A. 2015. Sedimentology and stable isotopes from a lacustrine-to-palustrine limestone deposited in an arid setting, climatic and tectonic factors: Miocene-Pliocene Opache Formation, Atacama Desert, Chile. Palaeogeography, Palaeoclimatology, Palaeoecology 426: 46-67. https://doi.org/10.1016/j.palaeo.2015.02.039

de Wet, C.; de Wet, A.; Godfrey, L.; Driscoll, E.; Patzskowsky, S.; Xu, C.; Gigliotti, S.; Feitl, M. 2019. Pliocene short-term climate changes preserved in continental lacustrine-palustrine carbonates: Western Opache Formation, Atacama Desert, Chile. Geological Society of America Bulletin 132: 1795-1816. https://doi.org/10.1130/B35227.1

de Wet, C.B.; Driscoll, E.; de Wet, A.; Godfrey, L.; Jordan, T.; Luethje, M.; Caterham, C.; Mortlock, R. 2022. Exceptional preservation in Quaternary Atacama Desert tufas: Evidence for groundwater and surface water in the Calama Basin, Atacama, Chile. The Depositional Record. https://doi.org/10.1002/dep2.221

Della Porta, G. 2015. Carbonate build-ups in lacustrine, hydrothermal and fluvial settings: comparing depositional geometry, fabric types and geochemical signature. *In* Microbial Carbonates in Space and Time: Implications for Global Exploration and Production (Bosence, D.; Gibbons, K.; Le Heron, D.; Morgan, W.; Pritchard, T.; Vining, B.; editors). Geological Society London, Special Publication 418: 17-68. London.

Dickson, J.A.D. 1966. Carbonate identification and genesis as revealed by staining. Journal of Sedimentary Petrology 36 (2): 491-505. https://doi.org/10.1306/74D714F6-2B21-11D7-8648000102C1865D

Duhart, P.; Muñoz, D.; Quiroz, D.; Mestre, A.; Varas, G. 2018. Carta Sierra Gorda, Región de Antofagasta. Servicio Nacional de Geología y Minería, Carta Geológica de Chile, Serie Geología Básica 198: 213 p. 1 mapa escala 1:100.000. Santiago.

Evenstar, L.A.; Hartley, A.J.; Archer, S.G.; Neilson, J.E. 2015. Climatic and halokinetic controls on alluvial-lacustrine sedimentation during compressional deformation, Andean forearc, northern Chile. Basin Research 28: 1-24. https://doi. org/10.1111/bre.12124

Fernández-Moreno, D.; Sánchez-Castillo, P.M.; Delgado, C.; Almeida, S.F.P. 2022. Diatom Species that Characterize

Saline Ponds (Southern Spain) with the Description of a New Navicula Species. Wetland Algae and Cyanobacteria 42 (1): 14.

Folk, R. 1994. Interaction between bacteria, nannobacteria, and mineral precipitation in hot springs of central Italy. Geographie physique et Quaternaire: 233-246. https://doi.org/10.7202/033005ar

Ford, T.D.; Pedley, H.M. 1996. A review of tufa and travertine deposits of the world. Earth-Science Reviews 41 (3-4): 117-175. https://doi.org/10.1016/S0012-8252(96)00030-X

Gerstenberger, H.; Haase, G. 1997. A highly effective emitter substance for mass spectrometric Pb isotope ratio determinations. Chemical Geology 136 (3-4): 309-312. https://doi.org/10.1016/S0009-2541(96)00033-2

Gibert, R.O.; Taberner, C.; Sáez, A.; Gipalt, S.; Alonso, R.N.; Edwards, R.L.; Pueyo, J.J. 2009. Igneous origin of CO_2 in ancient and recent hot-spring waters and travertines from the Northern Argentinian Andes. Journal of Sedimentary Research 79 (8): 554-567. https://doi.org/10.2110/jsr.2009.061

Godfrey, L.V.; Herrera, C.; Gamboa, C.; Mathur, R. 2019. Chemical and isotopic evolution of groundwater through the active Andean arc of northern Chile. Chemical Geology 518: 32-44. https://doi.org/10.1016/j.chemgeo.2019.04.011

Godfrey, L.V.; Herrera, C.; Burr, G.S.; Houston, J.; Aquirre, I.; Jordan, T.E. 2021. Delta ^{13}C and ^{14}C activity of groundwater DOC and DIC in the volcanically active and arid Loa Basin of northern Chile. Journal of Hydrology 595: 125987. https://doi.org/10.1016/j.jhydrol.2021.125987

Guo, L.; Riding, R. 1992. Aragonite laminae in hot water travertine crusts, Rapolano-Terme, Italy. Sedimentology 39 (6): 1067-1079. https://doi.org/10.1111/j.1365-3091.1992.tb01997.x

Guo, W.; Zhou, C. 2019. Triple oxygen isotope fractionation in the DIC-H_2O-CO_2 system: A numerical framework and its implications. Geochimica et Cosmochimica Acta 246: 541-564. https://doi.org/10.1016/j.gca.2018.11.018

Henríquez, S.; Becerra, J.; Arriagada, C. 2014. Geología del área San Pedro de Atacama, región de Antofagasta. Servicio Nacional de Geología y Minería, Carta Geológica de Chile, Serie Geología Básica 171. 1 mapa escala 1:100.000. Santiago.

Herrera, C.; Godfrey, L.; Urrutia, J.; Custodio, E.; Jordan, T.; JÃdar, J.; Delgado, K.; Barrenechea, F. 2021. Recharge and residence times of groundwater in hyper arid areas: The confined aquifer of Calama, Loa River Basin, Atacama Desert, Chile. Science of The Total Environment 752. https://doi.org/10.1016/j.scitotenv.2020.141847

Horwitz, E.P.; Chiarizia, R.; Dietz, M.L. 1992. A novel strontium-selective extraction chromatographic resin. Solvent Extr Ion Exch 10:313. Solvent Extraction and Ion Exchange 10 (2): 313-336. https://doi.org/10.1080/07366299208918107

Houston, J. 2007. Recharge to groundwater in the Turi Basin, northern Chile: An evaluation based on tritium and chloride mass balance techniques. Journal of Hydrology 334 (3-4): 534-544. https://doi.org/10.1016/j.jhydrol.2006.10.030

Houston, J. 2023. The providence and persistence of the perennial Rio Loa in the Atacama Desert: links between crustal processes and surface hydrology. Frontiers in Earth Science 11. https://doi.org/10.3389/feart.2023.1310088

Jones, B.; Renaut, R.W. 2008. Cyclic development of large, complex calcite dendrite crystals in the Clinton travertine, Interior British Columbia, Canada. Sedimentary Geology 203 (1-2): 17-35. https://doi.org/10.1016/j.sedgeo.2007.10.002

Jones, B.; Renaut, R.W. 2010. Calcareous spring deposits in continental settings. *In* Carbonates in Continental Settings: Facies, Environments and Processes, (Alonso-Zarza, A.M.; Tanner, L.H.; editors). Elsevier, Developments in Sedimentology 61: 177-224. Oxford.

Jordan, T.; Herrera, C.; Kirk-Lawlor, N.; Godfrey, L. 2015. Architecture of the aquifers of the Calama Basin, Loa catchment basin, northern Chile. Geosphere 11 (5): 1438-1474. https://doi.org/10.1130/GES01176.1

Kano, A.; Kawai, T.; Matsuoka, J.; Ihara, T. 2004. High-resolution records of rainfall events from clay bands in tufa. Geology 32 (9): 793-796. https://doi.org/10.1130/G20736.1

Kay, S.M.; Coira, B.; Caffe, P.J.; Chen, C.-H. 2010. Regional chemical diversity, crustal and mantle sources and evolution of central Andean Puna plateau ignimbrites. Journal of Volcanology and Geothermal Research 198 (1-2): 81-111. https://doi.org/10.1016/j.jvolgeores.2010.08.013

Kele S.; Breitenbach, S.F.; Capezzuoli, E.; Meckler, A.N.; Ziegler, M.; Millan, I.M.; Kluge, T.; Dea´k, J.; Hanselmann, K.; John, C.M.; Yan, H. 2015. Temperature dependence of oxygen-and clumped isotope fractionation in carbonates: A study of travertines and tufas in the 6-95 º C temperature range. Geochimica et Cosmochimica Acta 168: 172-192. https://doi.org/10.1016/j.gca.2015.06.032

Kim S.-T.; O'Neil J.R. 1997. Equilibrium and nonequilibrium oxygen isotope effects in synthetic carbonates". Geochimica et Cosmochimica Acta 61: 3461-3475. https://doi.org/10.1016/S0016-7037(97)00169-5

Kitano, Y. 1962. A study of the polymorphic formation of calcium carbonate in thermal springs with an emphasis on the effect of temperature. Bulletin of the Chemical Society of Japan 35 (12): 1980-1985. https://doi.org/10.1246/bcsj.35.1980

Lopez, B.; Camoin, G.; Ozkul, M.; Swennen, R.; Virgone, A. 2017. Sedimentology of coexisting travertine and tufa deposits in a mounded geothermal spring carbonate system, Obruktepe, Turkey. Sedimentology 64 (4): 903-931. https://doi.org/10.1111/sed.12284

Marohasy, J.; Abbot, J. 2015. Review of the salinity optima of the diatom Staurosirella pinnata: implications for water reform in Australia. WIT Transactions on Ecology and The Environment 196: 101-111.

Marquillas, R.; Sabino, I.; Sial, A.N.; del Papa, C.; Ferreira, V.; Matthews, S. 2007. Carbon and oxygen isotopes of Maastrichtian-Danian shallow marine carbonates: Yacoraite Formation, northwestern Argentina. Journal of South American Earth Sciences 23 (4): 304-320. https://doi.org/10.1016/j.james.2007.02.009

Martin-Bello, L.; Arenas, C.; Andrews, J.E.; Alonso-Zarza, A.M.; Marca, A. 2019. Lacustrine stromatolites as multi-scale recorders of climate change: Insights from the Miocene Ebro Basin. Palaeogeography, Palaeoclimatology, Palaeoecology 530: 312-329. https://doi.org/10.1016/j.palaeo.2019.05.001

Martini, I.; Capezzuoli, E. 2014. Interdigitated fluvial clastic deposits and calcareous tufa testifying an uplift of the catchment area: an example from the Pianizzoli area (southern Tuscany, Italy). Sedimentary Geology 299: 60-73. https://doi.org/10.1016/j.sedgeo.2013.11.001

Marx, A.; Dusek, J.; Jankovec, J.; Sanda, M.; Vogel, T.; van Geldern, R.; Hartmann, J.; Barth, J.A.C. 2017. A review of CO_2 and associated carbon dynamics in headwater streams: A global perspective. Reviews of Geophysics 55 (2): 560-585. https://doi.org/10.1002/2016RG000547

Matsuoka, J.; Kano, A.; Oba, T.; Watanabe, T.; Sakai, S.; Seto, K. 2001. Seasonal variation of stable isotopic compositions recorded in a laminated tufa, SW Japan. Earth and Planetary Science Letters 192 (1): 31-44. https://doi.org/10.1016/S0012-821X(01)00435-6

Matthews, S.J.; Marquillas, R.A.; Kemp, A.J.; Grange, F.K.; Gardeweg, M.C. 1996. Active skarn formation beneath Lascar Volcano, northern Chile: a petrographic and geochemical study of xenoliths in eruption products. Journal of Metamorphic Geology 14 (4): 509-530. https://doi.org/10.1046/j.1525-1314.1996.00359.x

May, G. 1997. Oligocene to recent evolution of the Calama Basin, Northern Chile. Ph.D. Thesis (Unpublished), University of Aberdeen, unpublished: 274 p.

May, G.; Hartley, A.; Stuart, F.; Chong, G. 1999. Tectonic signatures in arid continental basins: an example from the Upper Miocene-Pleistocene, Calama Basin, Andean Forearc, northern Chile. Palaeogeography, Palaeoclimatology, Palaeoecology 151 (1-3): 55-77. https://doi.org/10.1016/S0031-0182(99)00016-4

May, G.; Hartley, A.J.; Chong, G.; Stuart, F.; Turner, P.; Kape, S. 2005. Eocene to Pleistocene lithostratigraphy, chronostratigraphy and tectono-sedimentary evolution of the Calama Basin, northern Chile. Andean Geology 32: 33-58. http://dx.doi.org/10.5027/andgeoV32n1-a04

Minissale, A. 2004. Origin, transport and discharge of CO_2 in central Italy. Earth-Science Reviews 66 (1-2): 89-141. https://doi.org/10.1016/j.earscirev.2003.09.001

Minissale, A.; Kerrick, D.M.; Magro, G.; Murrell, M.T.; Paladini, M.; Rihs, S.; Sturchio, N.C.; Tassi, F.; Vaselli, O. 2002. Geochemistry of Quaternary travertines in the region north of Rome (Italy): structural, hydrologic and paleoclimatic implications. Earth and Planetary Science Letters 203 (2): 709-728. https://doi.org/10.1016/S0012-821X(02)00875-0

Parrish, J.T.; Hyland, E.G.; Chan, M.A.; Hasiotis. S.T. 2019. Stable and clumped isotopes in desert carbonate spring and lake deposits reveal palaeohydrology: A case study of the Lower Jurassic Navajo Sandstone, south-western USA. Sedimentology 66 (1): 32-52. https://doi.org/10.1111/sed.12540

Pedley, H.M. 1990. Classification and environmental models of cool freshwater tufas. Sedimentary Geology 68 (1-2): 143-154. https://doi.org/10.1016/0037-0738(90)90124-C

Pentecost, A. 2005. Travertine: Berlin, Springer Verlag: 445 p. Berlín.

Quade, J.; Rasbury, E.T.; Huntington, K.W.; Hudson, A.M.; Vonhof, H.; Anchukaitis, K.; Betancourt, J.; Latorre, C.; Pepper, M. 2017. Isotopic characterization of late Neogene travertine deposits at Barrancas Blancas in the eastern Atacama Desert, Chile. Chemical Geology 466: 41-56. https://doi.org/10.1016/j.chemgeo.2017.05.004

Romanek, C.S.; Grossman, E.L.; Morse, J.W. 1992. Carbon isotopic fractionation in synthetic aragonite and calcite - effects of temperature and precipitation rate. Geochimica et Cosmochimica Acta 56 (1): 419-430. https://doi.org/10.1016/0016-7037(92)90142-6

Romero, L.; Alonso, H.; Campano, P.; Fanfani, L.; Cidu, R.; Dadea, C.; Keegan, T.; Thornton, I.; Farago, M. 2003. Arsenic enrichment in waters and sediments of the Rio Loa (Second Region, Chile). Applied Geochemistry 18: 1399-1416. https://doi.org/10.1016/S0883-2927(03)00059-3.

Ryves, D.B.; Battarbee, R.W.; Fritz, S.C. 2006. The Dilemma of Disappearing Diatoms: Incorporating Diatom Dissolution Data into Paleoenvironmental Modeling and Reconstruction. Quaternary Science Reviews 28 (1-2): 120-136. https://doi.org/10.1016/j.quascirev.2008.08.021

Sáez, A.; Cabrera, L.; Garcés, M.; Bogaard, P.; Jensen, A.; Gimeno, D. 2012. The stratigraphic record of changing hyperaridity in the Atacama Desert over the last 10 Ma. Earth and Planetary Science Letters 355: 32-38. https://doi.org/10.1016/j.epsl.2012.08.029

Sawai, Y.; Nagumo, T.; Namegaya, Y.; Cisternas, M.V.; Lagos, M.; Shishikura, M. 2017. Diatom (Bacillariophyceae) assemblages in salt marshes of south-central Chile: Relations with tidal inundation time and salinity. Phycological Research 65: 29-37. https://doi.org/10.1111/pre.12156

Sellés, D.; Gardeweg, M. 2017. Geología del Área de Ascotán - Cerro Inacaliri, Región de Antofagasta, Santiago. Servicio Nacional de Geología y Minería, Carta Geológica de Chile, Serie Geología Básica 190: 73 p. 1 mapa escala 1:100.000. Santiago.

Stumm, W.; Morgan, J.J. 1995. Aquatic Chemistry: Chemical Equilibria and Rates in Natural Waters 3rd edition. Wiley: 1040 p. New York.

Tomlinson, A.J.; Blanco, P.N.; Dilles, J.H.; Maksaev, J.V. Ladino, U.M. 2018. Carta Calama, Región de Antofagasta. Servicio Nacional de Geología y Minería, Carta Geológica de Chile, Serie Geología Básica 199: 345 p. 1 mapa escala 1:100.000. Santiago.

Trabajo, R.; Rovira, L.; Wetzel, C.E.; Kelly, M.; Mann, D.G. 2013. Morphology and identity of some ecologically important small *Nitzschia* species. Diatom Research 28 (1). https://doi.org/10.1080/0269249X.2012.734531

Veizer, J. 1983. Trace elements and isotopes in sedimentary carbonates. *In* Carbonates: Mineralogy and Chemistry (Reeder, R.J.; editor). De Gruyter: 265-300. https://doi.org/10.1515/97815011508134-012

Veizer, J. 1989. Strontium isotopes in seawater through time. Annual Review of Earth and Planetary Science 17: 141-167.

Vermeesch, P. 2018. IsoplotR: A free and open toolbox for geochronology 9 (5): 1479-1493. https://doi.org/10.1016/j.gsf.2018.04.001

Wang, Z.; Jian-Jun, Y.; Hai, C.; Youfeng, N.; Meyer, M.C. 2022. Climatic Controls on Travertine Deposition in Southern Tibet during the Late Quaternary. Palaeogeography, Palaeoclimatology, Palaeoecology 589. https://doi.org/10.1016/j.palaeo.2022.110852

Winterer, E.L.; Sarti, M. 1994. Neptunian dykes and associated features in southern Spain: mechanics of formation and tectonic implications. Sedimentology 41 (6): 1109-1132. https://doi.org/10.1111/j.1365-3091.1995.tb00420.x

Wojtal, A.Z.; Sobczyk, L. 2012. The influence of substrates and physiochemical factors on the composition of diatom assemblages in karst springs and their applicability in water-quality assessment. Hydrobiologia 695: 97-108. https://doi.org/10.1007/s10750-012-1203-0

Zhou, G-T.; Zheng, Y-F. 2003. An experimental study of oxygen isotope fractionation between inorganically precipitated aragonite and water at low temperatures. Geochimica et Cosmochimica Acta 67 (3): 387-399.

Manuscript received: September 25, 2024; revised/accepted: November 21, 2025; available online: December 11, 2025.